Dynamics of ASC speck formation during skin inflammatory responses *in vivo*

1 Paola Kuri[1], Nicole L. Schieber[2], Thomas Thumberger[3], Joachim Wittbrodt[3], Yannick Schwab[2,4]
2 and Maria Leptin[1,5,6,*]

3 **Affiliations:**

4 [1]Directors' Research Unit, European Molecular Biology Laboratory (EMBL), Heidelberg, 69117
5 Germany
6 [2]Cell Biology and Biophysics Unit, European Molecular Biology Laboratory (EMBL),
7 Heidelberg, 69117 Germany
8 [3]Centre for Organismal Studies (COS), Heidelberg University, Heidelberg, 69120 Germany
9 [4]Electron Microscopy Core Facility (EMCF), European Molecular Biology Laboratory (EMBL),
10 Heidelberg, 69117 Germany
11 [5]Institute of Genetics, University of Cologne, Cologne, 50674 Germany
12 [6]EMBO, Heidelberg, 69117 Germany
13 *To whom correspondence should be addressed: Maria Leptin (maria.leptin@embo.org)

14 **One Sentence Summary**

15 With a new endogenous ASC real-time reporter we characterize speck dynamics *in vivo* as well as
16 the concomitant pyroptosis speck formation causes in keratinocytes.

17 **Abstract**

18 Activated danger or pathogen sensors trigger assembly of the inflammasome adaptor ASC into
19 specks, large signalling platforms considered hallmarks of inflammasome activation. Because a
20 lack of *in vivo* tools has prevented the study of endogenous ASC dynamics, we generated a live
21 ASC reporter through CRISPR/Cas9 tagging of the endogenous gene in zebrafish. We see strong
22 ASC expression in the skin and other epithelia that act as barriers to insult. A toxic stimulus
23 triggered speck formation and rapid pyroptosis in keratinocytes *in vivo*. Macrophages engulfed
24 and digested this speck-containing pyroptotic debris. A 3D ultrastructural reconstruction based on
25 CLEM of *in vivo* assembled specks revealed a compact network of highly intercrossed filaments,
26 whereas PYD or CARD alone formed filamentous aggregates. The effector caspase is recruited
27 through PYD, whose overexpression induced pyroptosis, but after substantial delay. Therefore,
28 formation of a single compact speck and rapid cell death induction *in vivo* requires full-length
29 ASC.

30 **Introduction**

31 Inflammasomes are large supramolecular structures that signal the detection of danger or
32 pathogenic stimuli by pattern recognition receptors, including some NOD-like receptor (NLR)
33 family members (*1*, *2*). Inflammasome signalling ultimately leads to the activation of the effector
34 caspase-1 through proximity-induced, auto-proteolytic cleavage (*3*). Activated caspase-1 can
35 proteolytically process cytokines as well as trigger pyroptosis, a pro-inflammatory form of
36 regulated cell death (*4*). During pyroptosis, cells swell after pores assemble in the plasma
37 membrane, leading to its rupture and the release of intracellular contents and membrane vesicles
38 (*5*, *6*). The adaptor molecule apoptosis-associated speck-like protein containing a CARD (ASC) is
39 central to the inflammasome assembly process (*7*). ASC is composed of two protein–protein
40 interaction domains of the death domain superfamily, a pyrin domain and a caspase activation and
41 recruitment domain (PYD_A and $CARD_A$, respectively) joined by a flexible linker (*8*). This enables
42 ASC to interact with both PYD-containing receptors and the CARD-containing pro-caspase-1,
43 thus bridging sensor and effector molecules (*1*).

44 Upon activation, inflammasome-forming receptors oligomerize and nucleate the prion-like
45 aggregation of ASC, enabling the subsequent clustering of caspase-1(*9*, *10*). During this process,
46 ASC is rapidly depleted from its steady-state homogeneous cellular distribution and self-
47 associates to form a single punctum inside the cell of about 1μm in diameter, called a speck (*11*,
48 *12*). The fast and irreversible assembly of ASC into specks maximizes the amount of activated
49 caspase-1, ensuring a high signal amplification (*1*, *13*).

50 Structural methods used to analyse specks *in vitro* showed that ASC assembles into filaments of
51 which PYD_A forms a rigid cylindrical core while $CARD_A$ is directed outwards through a flexible
52 attachment (*9*, *14*). The external orientation of $CARD_A$, in addition to enabling the recruitment of
53 downstream signalling elements, allows intra and inter-filament crosslinking through $CARD_A$-
54 $CARD_A$ interactions. Indeed, recent cell culture studies showed that preventing $CARD_A$
55 interactions by single point mutagenesis (*15*) or use of an intracellular alpaca antibody fused to a
56 fluorescent protein (*16*) abolishes speck formation, but not PYD_A filament assembly. However,
57 whether *in vivo* assembled specks also share this crosslinked filament arrangement remains to be
58 analysed with structural methods.

59 By expressing ASC fused to a fluorescent protein from a transgene, specks can be visualized by
60 light microscopy (*12*, *17*). The switch from a diffuse signal throughout the cell to one single
61 bright point is considered a readout and proxy for inflammasome activation (*18*-*21*). However,
62 experimentally expressed constructs increase the cellular concentration of ASC and, given the
63 protein's high tendency to aggregate if overexpressed (*7*), the risk that speck formation occurs

without an inflammatory stimulus also increases. The aforementioned study by Schmidt et al. (2016) represented the first time endogenous ASC was visible in a cell, but because speck formation is abolished by the use of the alpaca antibody, this tool cannot be used to assess speck formation *in vivo*.

Inflammasome function has mainly been studied in cells of the innate immune system such as macrophages. However, many pathogens and toxic agents first enter the body through epithelia that form the interfaces between body and environment, which evidently require innate immune surveillance mechanisms(*22*), but little is known about the role of the inflammasome and ASC in these, or other tissues such as endothelium or connective tissue which are also composed of cells that contribute to a global inflammatory response (*22-24*). For example, although ASC is present in mammalian epidermis (*25*) and it acts as a tumour suppressor in keratinocytes (*26*), whether speck formation leads to pyroptosis in these cells is unknown. Studying the responses of native tissues *in vivo* using murine models however, is challenging due to limited imaging accessibility. The zebrafish (*Danio rerio*) is a genetically and optically accessible model organism for studying diseases and for drug screening (*27-30*) in which *in vivo* innate immune responses can be studied in the context of a whole organism (*27*, *31*). The zebrafish genome contains more than ten times as many NLR genes as mice and humans (*32-34*), but it has only one gene encoding ASC (also called pycard) with a PYD-CARD domain structure (*35*).

We use zebrafish to study ASC function in tissues, such as the skin, in which inflammasome signalling has not been addressed *in vivo*. The transparency of the zebrafish makes this model especially well suited to study ASC-mediated inflammasome formation using speck formation as readout. For this purpose, we generated a line in which the endogenous *asc* is tagged with GFP using CRISPR/Cas9 technology, allowing body-wide *in vivo* analysis of speck formation.

This tool, together with an *asc* inducible expression system with which we visualize the ultrastructure of specks formed *in vivo*, revealed that speck formation in keratinocytes can occur within the nucleus and that macrophages engulf pyroptotic cellular debris. Furthermore, the expression of the separate ASC domains shows both PYD_A and $CARD_A$ cluster in filamentous aggregates. PYD_A aggregates are sufficient to elicit cell death at a reduced rate, showing $CARD_A$ is required both for maximal speck clustering and cell death efficiency. Finally, by generating a Caspase-1 orthologue knockout, we conclude that speck formation unleashes Caspase-dependent pyroptosis in keratinocytes *in vivo*.

Results

Tissue specific expression of ASC

97 ASC has been shown to be expressed in the skin, digestive tract, bone marrow and peripheral
98 blood leukocytes, among other tissues in humans (*36*), and most myeloid lineage cell lines also
99 express *asc* constitutively (*7*). However, no encompassing analysis addressing the spatial
100 distribution of its expression sites within an organism has been made. To investigate the role of
101 ASC *in vivo* we first characterized gene and protein expression in zebrafish by Reverse
102 Transcription PCR, *in situ* hybridisation and immunofluorescence with a newly generated
103 antibody against zebrafish ASC. The expression of *asc* is detectable from the morula stage
104 onward, and adult hematopoietic tissues also express *asc* (Fig. S1A). In 3 dpf larvae, *asc* RNA is
105 present throughout the epidermis and in the area around the gills (Fig. 1A and fig. S1B), where it
106 has previously been reported to have a role in pharyngeal arch development (*35*). Sections
107 showed expression in internal tissues such as the intestinal epithelium and individual *asc*-
108 expressing cells in the brain (Fig. 1B-C and fig. S1C-G"). The lateral line system and some
109 internal tissues, such as the notochord and muscle, lacked ASC. Immunostainings showed ASC's
110 presence in the epidermis from 1 to at least 5 dpf (Fig. S1I-O). Transgenic tissue-specific markers
111 identified the ASC-expressing cells in the skin as both enveloping layer (EVL) and basal
112 keratinocytes (Fig. 1D and D' and fig. S1P). In these cells the protein is seen both in the
113 cytoplasm and the nucleus (Fig. 1E and fig. S1P). All macrophages express ASC, as do most
114 neutrophils (Fig. 1F and G), but not all cells labelled by the myeloid lineage reporter *pU1* express
115 ASC (Fig. 1H).

116 ***Endogenous ASC and specks visualized in vivo in a knockin transgenic line***

117 To be able to study ASC *in vivo* we generated a transgenic CRISPR knockin line through
118 homology-dependent repair in which the endogenous protein is fused with GFP, called
119 *Tg(asc:asc-EGFP)* (Fig. S2A-D). In agreement with the above results, transgenic embryos have
120 ASC-GFP throughout the entire epidermis in nuclear and cytoplasmic compartments as well as in
121 the intestinal epithelium (Fig. 2A-B" and fig. S2E-G). ASC-GFP is also expressed in myeloid
122 cells (Fig. 2C). Microglia, the tissue-resident macrophages of the brain (*37*) were ASC positive as
123 were cells in the caudal hematopoietic tissue, many (but not all) of which were labelled by the
124 *pU1* reporter transgene. At all stages examined, muscle cells and other internal tissues were
125 devoid of GFP.
126 We observed the sporadic appearance of GFP specks in the epidermis of *Tg(asc:asc-EGFP)*
127 larvae (Movie S1). Without exception, specks were contained in dead or dying cells, as shown in
128 brightfield images where these cells were rounded and dislodged from the rest of the epithelium
129 (Fig. 2D-F). The reason for spontaneous speck formation in these examples is unclear. To

130 determine if inflammatory stimuli could trigger speck formation in epidermal cells, we exposed
131 *Tg(asc:asc-EGFP)* embryos to high concentrations of copper sulphate ($CuSO_4$), a compound
132 toxic to zebrafish larvae (*38-40*). The epidermis of these larvae showed signs of stress, with many
133 deformed cells forming a rugged instead of smooth epithelium, and had significantly increased
134 numbers of specks (Fig. 2G and G'). Cells containing a speck were rounded and dislodged from
135 the rest of the epithelium, which is indicative of cell death. However, not all abnormal epidermal
136 cells had specks (Fig. 2G''), suggesting $CuSO_4$ exposure triggers a range of stress symptoms, and
137 speck formation may occur as an indirect consequence of $CuSO_4$-induced toxicity to the skin.
138 Because toxicity-induced speck formation in the skin resulted in undesired side effects, making
139 this an inadequate system in which to address the dynamics and consequences of speck formation
140 *in vivo*, we tested other more direct means of triggering speck formation.

141 ***Speck formation in vivo is induced by NLR or ASC overexpression***

142 When ASC is present at endogenous concentrations, activated members of the NLR protein
143 family, among other receptors, can trigger speck formation. Under overexpression conditions,
144 however, the propensity of ASC to spontaneously aggregate in cultured cells is well documented
145 (*11*, *18*, *19*). We therefore tested whether these stimuli resulted in speck formation in live fish.
146 Overexpressing a PYD-containing zebrafish NLR lacking the LRR domain led to ASC-GFP
147 speck formation in epidermal cells of the *Tg(asc:asc-EGFP)* line, showing that the GFP-tagged
148 endogenous ASC responds appropriately to its direct stimulus (Fig. 3A and Movie S2). We also
149 used an overexpression system based on a construct, *HSE:asc-mKate2,* in which mKate2-tagged
150 ASC is expressed under the control of a heat shock promoter (*41*) that allowed us to induce ASC
151 expression throughout the fish, including cells that do not endogenously express it. Transient
152 expression of ASC-mKate2 from this construct led to the appearance of specks, whereas mKate2
153 alone had a cytoplasmic distribution (Fig. S3A). Speck formation was not caused by the mKate2
154 fused to ASC, nor by heat shock-related stress, since overexpressing ASC with other tags and
155 using other expression systems also resulted in speck formation (Fig. S3B-D). To simultaneously
156 and stably induce ASC-mKate2 overexpression in all cells we generated the transgenic line
157 *Tg(HSE:asc-mKate2)* (Fig. 3B). A quantification of speck formation over time in transgenic
158 embryos shows that from 2.5h post heat shock (2.5 hphs) the number of specks increases rapidly
159 and plateaus at around 17 hphs (Fig. 3C and Movie S3). Each cell formed only one speck,
160 concomitant with the depletion of the cytoplasmic pool of ASC-mKate2 (Fig. 3D and Movie S3).
161 Although muscle cells do not express *asc* endogenously, the heat shock-induced ASC-mKate2
162 also assembled into a single speck in these cells. When we overexpressed ASC-mKate2 in

163 *Tg(asc:asc-EGFP)* embryos, specks that formed in muscle cells were constituted exclusively by
164 ASC-mKate2 (Fig. 3E), whereas in epidermal cells, the endogenous ASC-GFP was recruited to
165 the ASC-mKate2 speck (Fig. 3F and Movie S2). These results suggest that overexpression of
166 ASC or its upstream receptors trigger speck formation and bypass the need for an inflammatory
167 stimulus to activate inflammasome signalling.

168 ***Specks are formed by large filamentous assemblies of ASC***

169 Based on cryo-EM structures of *in vitro* assembled PYD_A filaments and EM data of ASC specks
170 reconstituted *in vitro* (*9*), specks are thought to be composed of crosslinked filaments that
171 aggregate into a sphere (*42*). To characterize the structure of *in vivo*-formed specks, we used
172 correlative light and electron microscopy (CLEM) (Fig. 4A and B, and fig. S4A). We visualized
173 ultrastructural details of specks formed in muscle cells after inducing ASC-mKate2 expression in
174 the *Tg(HSE:asc-mKate2)* line. Specks in muscle cells form a cluster of 700 nm in diameter
175 consisting of highly intercrossed filaments (Fig. 4C, fig. S4B and Movie S4). A three-dimensional
176 model of the filaments reveals that the aggregated ASC filaments form a globular structure (Fig.
177 4D). This data is a strong indication that the filamentous organization observed from *in vitro*
178 studies is also true of *in vivo* assembled specks.

179 ***Mutating conserved predicted phosphorylation sites abrogates speck formation***

180 Activation of ASC, like other inflammasome components, is subjected to regulation by
181 posttranslational modifications (*7*). Thus, the speck formation we observe should depend on these
182 as well. We used the overexpression system to test whether ASC in zebrafish was regulated
183 through phosphorylation by the c-Jun N-terminal kinase (Jnk) and spleen tyrosine kinase (Syk)
184 signaling pathways, as reported for mammalian ASC (*43*, *44*). An *in silico* analysis, as used by
185 Hara et al. (2013), predicted a number of potential Jnk and Syk phosphorylation sites in zebrafish
186 ASC (Table S1). Three corresponded to residues within the $CARD_A$ that are conserved in mouse
187 and human ASC (Fig. 4E and F). We mutated these three sites (Y152F, T160F and T170A) and
188 one additional site in PYD_A, which was not conserved (T38A). Since muscle cells do not express
189 *asc* endogenously we were able to use these cells for an *in vivo* analysis of speck formation by
190 mutant proteins while avoiding interference from the wild type ASC. Transiently expressed ASC-
191 mKate2 containing the four mutations formed a striated pattern or large filamentous aggregates in
192 muscle cells, rather than a compact speck (Fig. 4G). By expressing constructs with single
193 mutations, we found that the Y152F mutation was sufficient to disrupt speck formation entirely
194 (Fig. 4H), similar to the corresponding mutations in mouse (Y144A) or human ASC (Y146A)

195 which also caused defective speck formation (*43*, *44*). These results support the notion that speck
196 formation caused by the experimental conditions used here is under the control of conserved ASC
197 post-translational regulatory mechanisms and assembly therefore follows the physiological
198 signalling pathway.

199 ***Speck formation leads to keratinocyte pyroptosis***

200 It is well established that speck formation can cause cell death by pyroptosis in macrophages in
201 culture. However, the first barrier a pathogen must overcome to establish infection are epithelial
202 surfaces that cover the body, which, as we have shown, express high levels of ASC. Yet, very
203 little is known about the function and dynamics of ASC activation and speck formation in this
204 important tissue. Since inducing *asc* expression in the *Tg(HSE:asc-mKate2)* line allows us to
205 study cell-type specific responses to speck formation, we compared responses of keratinocytes,
206 which endogenously express *asc*, to muscle cells, which do not. We observed starkly different
207 responses to speck formation. Keratinocytes round up within minutes after speck formation,
208 whereas muscle cells show no visible change over at least 10 hours, during which the speck
209 continuously increases in size (Fig. 5A and Movie S5). The response in epidermal cells was
210 independent of the method used to overexpress ASC (Fig. S4C). That the appearance of ASC-
211 mKate2 specks is associated with the same morphological changes as those seen after the
212 formation of endogenous ASC-GFP specks suggests that inflammasome signalling is being
213 activated in these cells as a result of overexpression-induced speck formation.
214 We quantified cell death in the *Tg(HSE:asc-mKate2)* line by using acridine orange (Fig. 5B).
215 Before specks assemble, *Tg(HSE:asc-mKate2)* and control larvae show similar levels of staining.
216 However, after speck formation, cell death was significantly higher in heat shocked transgenic
217 larvae (Fig. 5C). Most of the acridine orange staining was located in the skin (Fig. S4D); and
218 keratinocytes, but not muscle cells, accumulated acridine orange in their surroundings after speck
219 formation (Fig. S4E). This, together with the observed changes in morphology, suggested that
220 keratinocytes were undergoing cell death upon speck formation. To test this, we monitored the
221 cellular changes in response to speck formation specifically in EVL keratinocytes using
222 *Tg(krt4:GFP, HSE:asc-mKate2)* larvae (Fig. 5D and Movie S5). All GFP-positive cells that
223 formed a speck showed classic signs of pyroptosis (*6*) less than 15 minutes after speck formation,
224 including rounding up, detachment from the epithelia and loss of plasma membrane integrity. We
225 analysed the process of cell extrusion by labelling the plasma membrane with a membrane-
226 targeted GFP (lynGFP) and observed that speck formation led to extrusion of the pyroptotic cell
227 from the epithelial sheet, with surrounding cells sealing the gap (Fig. 5E and Movie S5). This was

228 also seen after transient overexpression of ASC-tGFP in a reporter line labelling the membranes
229 of keratinocytes (Fig. S4F and Movie S5). These results show that keratinocytes undergo
230 pyroptosis within 15 min of speck formation.

231 ***Effect of speck formation by nuclear ASC***

232 Both when detected by antibodies and tagged by GFP, endogenous ASC is present in the
233 cytoplasm and the nucleus. Either pool can form specks in HeLa cells (*17*), although the
234 significance of this, and in particular, whether both nuclear and the cytoplasmic specks can induce
235 cell death *in vivo*, is unclear. To test this, we transiently expressed a nuclear-targeted ASC-
236 mKate2 (NLS-ASC-mKate2) in the *Tg(asc:asc-EGFP)* line, which would allow us to monitor not
237 only the effect of nuclear ASC, but also the endogenous nuclear and cytoplasmic ASC pools.
238 When NLS-ASC-mKate2 formed specks in the nucleus of ASC-GFP expressing keratinocytes,
239 these cells underwent cell death with the same dynamics as described above. Cell death occurred
240 without the recruitment of the cytoplasmic pool of the endogenous ASC-GFP (Fig. 6A and Movie
241 S6). Therefore, the presence of a nuclear speck is sufficient, and neither the depletion of the
242 cytoplasmic pool nor a cytoplasmic speck is required for keratinocyte pyroptosis. However, in
243 cases where the nuclear envelope became permeable to the endogenous ASC-GFP before death
244 occurred, the cytoplasmic pool of ASC-GFP was also recruited to the nuclear speck (Fig. 6B-E).
245 In cases where the plasma membrane collapsed prior to nuclear envelope breakdown, cytoplasmic
246 ASC-GFP leaked to the extracellular environment before it was recruited to the nuclear speck
247 (Fig. 6F-I). Similar results were obtained by transiently coexpressing ASC-mKate2 with GFP in a
248 transgenic line carrying the *βactinNLS-tagBFP* transgene to label all nuclei (Fig. S5 and Movie
249 S6). Namely, specks assembled either from the cytoplasmic or the nuclear pool of ASC, but
250 regardless of the compartment in which the speck formed its assembly led to cell death. This
251 confirms that speck formation in the nucleus is sufficient to trigger pyroptosis in keratinocytes.

252 ***Clearance of pyroptotic debris containing ASC specks by macrophages***

253 After macrophages undergo pyroptosis, they leave behind a structure composed of ruptured
254 plasma membrane containing insoluble contents called "pore-induced intracellular traps (PITs)".
255 In culture, neighbouring phagocytes clear up PITs through efferocytosis (*45*). There is also
256 evidence that ASC specks are released to the extracellular space and can spread inflammation by
257 recruiting the soluble ASC in the cytoplasm of phagocytes that engulf them (*46*, *47*). However,
258 whether ASC specks remain trapped in PITs, and the rules that determine when engulfed specks
259 induce speck formation and pyroptosis in the phagocyte have yet to be defined. We observed that,
260 after keratinocyte cell death, specks remained enclosed within the cellular debris (Fig. 2E and F

261 and fig. 5A). To test whether phagocytes could engulf speck-containing cellular debris, we
262 induced ASC-mKate2 expression in the *Tg(HSE:asc-mKate2)* line crossed with the macrophage
263 reporter line. Macrophages were indeed capable of engulfing pyroptotic debris with specks (Fig.
264 6J and Movie S7). Instances of macrophages containing multiple phagosomes with specks
265 suggest there is continuous uptake of speck-containing debris by phagocytes, and that engulfed
266 specks do not elicit a pyroptotic response in the macrophages within 2-3 hours after engulfment.
267 Instead, the gradual loss of fluorescence from phagocytized ASC-mKate2 specks suggests that
268 macrophages are capable of digesting specks after engulfment (Fig. S6 and Movie S7). Thus, the
269 main function of phagocytes that we observe *in vivo* is to clear speck-containing pyroptotic
270 cellular debris, and we have seen no incidences of specks triggering further death after
271 engulfment.

272 ***Domain requirements for compact speck clustering and efficient cell death***

273 Based on *in vitro* and cell culture experiments, the PYD and CARD domains of ASC are thought
274 to have distinct roles during speck formation, with PYD_A assembling into filaments that are
275 crosslinked by inter-filament CARD interactions (*15*). To determine each domain's role in speck
276 assembly and pyroptosis *in vivo* we overexpressed the single PYD_A and $CARD_A$ fused to mKate2
277 (PYD_A-mKate2 and $CARD_A$-mKate2, respectively). In muscle cells, PYD_A most frequently
278 assembled into long filamentous structures, whereas $CARD_A$ aggregated into smaller punctate
279 aggregates throughout the cell (Fig. 7A). In contrast, expression of either domain keratinocytes
280 resulted in the formation of a normal-looking compact speck that led to pyroptosis (Fig. S7A and
281 B, and Movie S8). The most likely reason for this difference is the presence of endogenous ASC
282 in keratinocytes. To test this, we repeated these experiments under conditions of *asc* morpholino
283 knockdown (Fig. S7C). While overexpressed ASC*-mKate2 under *asc* knockdown conditions
284 formed compact specks in keratinocytes and caused cell death (Fig. S7D and Movie S8), as
285 observed in control larvae, overexpressed PYD^*_A or $CARD_A$ failed to do so. Instead, following a
286 slower depletion of the cytoplasmic pool of the protein than that of full-length ASC, the single
287 domains formed aggregates similar to those assembled in muscle cells (Fig. 7B and C and Movie
288 S8). The formation of these aggregates was not associated with immediate cell death: PYD_A-
289 expressing epidermal cells died over 2 hours after PYD_A-aggregates are first seen whereas cells
290 with $CARD_A$ aggregates survived for more than 10 hours after aggregate formation. This differs
291 from the fast response observed within ~10 min of ASC-mKate2 speck formation in *asc*
292 knockdown larvae. PYD_A is therefore both necessary and sufficient for cell death, which suggests
293 that this domain mediates the interaction with downstream elements that trigger pyroptosis.

294 ***PYD-dependent recruitment of Caspa to the ASC speck***

295 In mammals, the effector domain of ASC for triggering pyroptosis is the CARD, which interacts
296 with the CARD of Caspase1. For this reason, it is surprising that in zebrafish PYD appears to be
297 the effector domain. We therefore tested whether caspases were involved in the response to speck
298 formation, and if so, how they interacted with ASC. Treatment of *Tg(HSE:asc-mKate2)* larvae
299 with the pan-caspase inhibitor (Q-VD-OPh hydrate) resulted in a significant reduction in cell
300 death without affecting speck formation (Fig. 8A and B), showing that caspase activity is required
301 for ASC-dependent pyroptosis. Since caspases are recruited to the speck for auto-activation (*4*),
302 we tested which caspases could interact with the ASC speck. There are two homologues of
303 mammalian *caspase-1* in zebrafish, *caspa* and *caspb*, both with N-terminal PYD domains. We
304 generated GFP fusions for both caspases, as well as for *casp3a*, the zebrafish orthologue of
305 mammalian Caspase-3, and transiently coexpressed them with ASC-mKate2. Only Caspa was
306 recruited to ASC specks assembled in muscle cells (Fig. 8C). By expressing the PYD and p20-
307 p10 domains of Caspa (PYD_C and p20-p10) separately with either the PYD_A or $CARD_A$, we
308 confirmed that the interaction occurs via the PYD domains of both proteins (Fig. 8D and fig.
309 S8A-C).
310 Transient overexpression of Caspa, unlike that of Caspb or Casp3a, was extremely toxic to
311 epidermal cells (Fig. S8D). Caspa-GFP-overexpressing embryos lacked normal-looking
312 keratinocytes with homogeneous GFP expression, and instead had copious green-labelled cellular
313 debris. Even muscle cells, which were not affected by ASC speck formation, displayed signs of
314 damage after Caspa expression (Fig. S8E). Considering that endogenous *caspa* is expressed in the
315 skin (Fig. 8E and fig. S8F) these data strongly suggest that Caspa is the effector caspase
316 activating pyroptosis in keratinocytes after speck formation and that muscle cells are protected
317 from speck-induced pyroptosis because they do not express it.
318 To test this hypothesis, we generated a *caspa* mutant by use of CRISPR/Cas9 and identified two
319 mutations ($caspa^{K**}$ and $caspa^{\Delta 800}$) that resulted in transcripts with a nonsense codon within the
320 first exon (Fig. S8G-J). We transiently expressed ASC-mKate2 and GFP in *caspa* knockout
321 larvae. Speck formation in keratinocytes proceeded normally in these larvae, but did not result in
322 pyroptosis with cells instead surviving for hours after speck formation (Fig. 8F and Movie S9).
323 Eventually, keratinocytes with specks displayed cellular blebbing, nuclear condensation and
324 slowly disintegrated into vesicles strongly reminiscent of apoptotic bodies, suggesting that if
325 Caspa is absent, speck formation results in activation of apoptosis instead of pyroptosis. These
326 results establish Caspa as the direct and only downstream effector of ASC speck formation
327 driving immediate pyroptosis *in vivo*.

328 **Discussion**

329 ASC speck formation is a hallmark of inflammasome activation. The use of cell lines has
330 significantly contributed to dissect the molecular interactions involved in this signalling cascade
331 but we lack deeper understanding of how inflammasome activation occurs in cells within their
332 native environment. This knowledge gap can be bridged by using models that enable visualization
333 of immune processes in the context of the whole organism (*27*, *30*). Previous studies had
334 suggested that some elements of the inflammasome signalling cascade are involved in the defence
335 against pathogens using zebrafish infection models (*48-50*) and it was recently shown that
336 zebrafish lacking ASC are more susceptible to *Salmonella* Typhimurium infection (*51*). In our
337 case, a live imaging approach allowed us to characterize inflammasome signalling in the skin *in*
338 *vivo*. In both fish and mammals, the skin functions as an immune organ that provides a crucial
339 protective barrier (*52*). Keratinocytes both relay environmental signals to immune cells and
340 execute a response themselves, with their death acting as a potent trigger of skin inflammation
341 (*23*, *53*). Inflammasome activation in keratinocytes has been implicated in response to a number
342 of stimuli (*25*, *54-58*) and the strong expression of ASC we observe in the skin, as well as other
343 epithelia like gills and intestine suggested that the activation of inflammasome is of particular
344 importance in these tissues. Our finding that keratinocytes respond to inflammatory conditions by
345 forming ASC specks and triggering pyroptosis, underscores the relevance of inflammasome
346 signalling in epithelia *in vivo*.
347 Our work shows that the specific structural mechanisms that lead to ASC's assembly into specks
348 are conserved between zebrafish and mammals. First, several different ways of overexpressing
349 ASC *in vivo* confirm its high tendency for aggregation, consistent with previous examples
350 showing zebrafish ASC specks in mammalian cells (*35*) and in uninfected control zebrafish larvae
351 injected with *asc-GFP* mRNA (*49*). Second, the abrogation of speck formation when predicted
352 conserved phosphorylation sites of zebrafish ASC are mutated suggests conservation of Jnk and
353 Syk-dependent posttranslational regulatory mechanisms of ASC (*43*, *44*). Lastly, our CLEM
354 analysis, which constitutes the first structural analysis of *in vivo* specks, shows its clustered
355 filamentous nature and confirms the model based on *in vitro* inflammasome reconstitutions
356 depicting a speck as a three-dimensional globular ultrastructure composed of multiple highly
357 intercrossed filaments (*9*).
358 An important difference between mammalian and zebrafish ASC is the domain that interacts with
359 the effector caspase. In contrast to the mammalian inflammasome, in which Caspase-1 and ASC
360 interact via their CARD domains, zebrafish Caspa, which has an N-terminal PYD instead of a

361 CARD, is recruited to the ASC speck via its PYD domain, in agreement with previous
362 mammalian cell culture experiments (*35*). $CARD_A$ in mammals is located on the surface of ASC
363 filaments, enabling the recruitment of Caspase-1. Since CARD domains can themselves assemble
364 into filaments, as in the case of MAVS in RIG-I antiviral signalling (*59*) the ASC filament
365 domain structure may be inverted in zebrafish, allowing the PYD to interact with Caspa.
366 Our results on the effects of expressing the individual domains of ASC reveal a correlation
367 between the compaction of the ASC speck and the efficiency with which it leads to cell death.
368 Both PYD_A and $CARD_A$ alone have the capacity to aggregate when overexpressed, but neither
369 cluster in a single compact speck. $CARD_A$ aggregates have no detrimental effect on cells, but
370 overexpression of only PYD_A whose aggregates are able recruit Caspa, results in cell death.
371 Therefore, in this setup, neither the association of CARD and PYD, nor the formation of a
372 compact speck, nor the bridging of PYD to other molecules via CARD, are essential for cell death
373 as such. Instead, it appears that the PYD-mediated recruitment of Caspa is sufficient. However,
374 the finding that the rate of aggregation and cell death are significantly reduced indicates that
375 $CARD_A$ is needed for the highly efficient and rapid triggering of pyroptosis. This could be
376 achieved by maximizing speck compaction though filament crosslinking, as shown in cell culture
377 (*15*, *16*), which might cause more rapid and efficient nucleation and clustering of Caspa than
378 PYD aggregates, by recruiting additional accessory molecules to the speck that accelerate Caspa
379 activation, or through a combination of both mechanisms.
380 Specks had been shown to remain as stable aggregates in the extracellular space after ASC
381 overexpression in COS-7 cells and in the supernatant of macrophage cell cultures upon exposure
382 to inflammasome-activating stimuli (*46*, *47*, *60*). In the *Tg(HSE:asc-mKate2)* line, ASC specks
383 persist after the death of the cells and appear to remain associated with the pyroptotic cellular
384 debris, which can be readily engulfed by macrophages, as is the case in culture for *in vitro*
385 assembled specks (*47*) and PITs (*45*). Macrophages *in vivo* continuously cleared up speck-
386 containing cellular debris, and a single macrophage could contain multiple phagosomes with
387 specks. Furthermore, engulfment led to the degradation of the specks within phagosomes.
388 Franklin et al. (2014) reported that macrophages that engulfed *in vitro* assembled specks could
389 undergo pyroptosis after the speck was released into the cytosol and nucleated clustering of the
390 phagocytes' soluble ASC (*47*), an observation which is supported by recent *in vivo* data (*61*).
391 However, we did not find that a macrophage's ability to clear up debris *in vivo* diminished or that
392 the macrophage was affected by the engulfment of a speck short term. It is possible that specks
393 enclosed within ruptured membranes are less efficient triggers of the phagolysosomal damage
394 that releases them into the cytosol; or that, *in vivo*, additional conditions are required to activate

395 this mechanism of signalling spreading, such as extraordinarily high or sustained organismal
396 inflammation levels. This would explain why extracellular specks are detected in the case of
397 chronic, but not acute inflammation (*47*).
398 We noticed that not all specks that form in the epidermis are removed. Keratinocytes belonging to
399 the outer epidermal layer (EVL), marked by the *krt4* transgene, are extruded from the epithelium
400 towards the outside of the body. Since they are sloughed off and become separate from the living
401 tissue, macrophages are likely unable to reach and remove their cellular debris.
402 Recently, speck formation within a tissue was visualized by intravital imaging of macrophages
403 derived from retrovirally transduced ASC-GFP hematopoietic stem cells in bone marrow
404 chimeric mice (*61*). A second study generated a transgenic mouse carrying ASC-citrine that can
405 be expressed in a lineage-specific manner (*21*). Although both studies analyse inflammasome
406 activation within a living tissue, they rely on the insertion of an additional copy of ASC-FP
407 expressed under viral promoters for protein visualization; thus, expression levels from the
408 transgene are artificial, and cells that endogenously express *asc* will therefore have an increased
409 concentration of the protein. These disadvantages are circumvented by endogenous tagging of
410 *asc*, as in the *Tg(asc:asc-EGFP)* line, in which ASC-GFP is only present in cells where it is
411 endogenously expressed and at physiological levels, thus avoiding activation artefacts. We cannot
412 entirely exclude that the GFP itself influences the behaviour of the protein, but this would be a
413 caveat affecting all studies using fluorescent proteins to visualize ASC live. However, since
414 endogenous inflammasome activation in the context of organismal infection has not been studied
415 live, we believe that the *Tg(asc:asc-EGFP)* line will prove a valuable tool to address this question
416 *in vivo*.

417 **Experimental Procedures**

418 ***Imaging***

419 For confocal microscopy, larvae were anesthetized with MESAB (ethyl-m-aminobenzoate
420 methanesulfonate) by adding the compound to the media at a concentration of 40 µg/ml and
421 mounted in 1.3% low-melting point agarose (Peqlab). Imaging of immunostainings was carried
422 out in a Leica SP8 TCS confocal microscope using dry 20x/0.8 or water 40x/1.1 objectives. Live
423 imaging was performed using Zeiss LSM 780 confocal microscope at room temperature. For
424 time-lapse imaging of epidermal and muscle cells, a 40x water objective was used (LD C-
425 Apochromat 40x/1.1 W Corr M27 or C-Apochromat 40x/1.2 W Corr M27, Zeiss). Whole larvae

426 were imaged using a 5x (Plan-Apochromat 5x/0.16 M27, Zeiss) or 10x (Plan-Apochromat
427 10x/0.45 M27, Zeiss) as tiles and later stitched.

428 ***asc knockdown***

429 Design and synthesis of *asc* ATG morpholino (5'- GCTGCTCCTTGAAAGATTCCGCCAT-3')
430 was carried out by Gene Tools, LLC. Stock morpholino was and diluted in nuclease-free H_2O to a
431 concentration of 3 mM and stored at room temperature. For knockdown experiments, morpholino
432 was injected at a concentration of 0.6 mM. Morpholino was validated by immunostaining and, for
433 *in vivo* experiments, by loss of fluorescence after injection in homozygous *Tg(asc:asc-EGFP)*
434 embryos.

435 ***Generation of asc:asc-EGFP line***

436 *sgRNA design:* Guide RNAs that targeted the last exon of *asc* (ENSDARG00000040076) were
437 designed using the CRISPR/Cas9 target online predictor CCTop (http://crispr.cos.uni-
438 heidelberg.de) (*62*). Two suitable hits, Guide 1 (ATTCCTGATGGATGACCTTG) and Guide 2
439 (ATCTTCACTCAGCATCCTCA) were synthetized using the oligo annealing method into vector
440 DR274. DR274 was a gift from Keith Joung (Addgene plasmid #42250) (*63*). *sgRNA in vivo*
441 *validation:* to test whether sgRNAs Guide 1 and 2 targeted the region of interest *in vivo*, they
442 were individually injected in varying concentrations (15-150 ng/µl) together with 1 µl of Cas9
443 protein (4 mg/ml) complemented with ca. 150 mM KCl into fertilized eggs at the one-cell stage of
444 the zebrafish TLF strain. Successful knockdown was verified by sequencing of a 1.3 kb PCR
445 product from the targeted region of *asc* (Fwd: CCTGTCTGACCATGTGAACATCTA, Rev:
446 TTAGCATTTGTCCTTATCGCAAAC). *Donor vector construction:* Donor vectors were
447 constructed via Golden GATEway cloning (*64*). In short, 50 ng of entry vector (EV) plasmids
448 numbered 1 to 6 and a vector backbone, were digested with 0.5 µl of *Bsa*I (Fast Digest, Thermo
449 Fisher Scientific) and ligated with 0.5 µl of T4 DNA Ligase (30 U/µl, Thermo Fisher Scientific)
450 in several rounds in one continuous reaction of 10 cycles consisting of 30 min at 37°C and 20 min
451 at 16°C, followed by 5 min of 50°C and 5 min of 80°C to inactivate both enzymes. EV1 included
452 a donor plasmid specific target site for *in vivo* plasmid linearization
453 (GGCGAGGGCGATGCCACCTACGG) (*62*), EV3 contained an *EGFP* CDS with a flexilinker
454 for tagging of *asc*, EV4 was empty and EV6 contained a STOP codon. Homology 5' and 3' flanks
455 of different lengths (1 kb for 5' and 1 kb or 2 kb for 3') were amplified from zebrafish gDNA and
456 cloned into empty EV2 and EV5. Flanks were amplified and designed according to the specific
457 Cas9 cleavage sites for Guide 1 and Guide 2 as previously reported (*65*) to increase chances of
458 precise integration. All vectors whose cloning is not mentioned were kindly provided by the

459 Wittbrodt lab. *Injection:* For homologous recombination, the *asc* sgRNA Guide 1 or 2 (120 ng/µl)
460 and a corresponding donor vector (20-50 ng/µl) were injected with a donor specific sgRNA for
461 donor *in vivo* plasmid linearization (150 ng/µl) and 1 µl of Cas9 protein (4 mg/ml) in a solution
462 complemented with ca. 150 mM KCl. *Screening:* Larvae were screened at 2 dpf for GFP
463 expression. We observed higher successful recombination rates when using *asc* Guide 2 and a
464 donor vector with 5' and 3' homology flanks of 1 and 2 kb, respectively. However, the number of
465 positive embryos was low and highly variable, ranging from 1 in 40 to 1 in 200 injected embryos.
466 In total, 18 positive F0 larvae were raised into adulthood and screened for positive integration in
467 the germline by outcrossing with wild type fish. One founder whose F1 progeny carried an allele
468 with a correct insertion of *linker-EGFP* cassette at a rate of 30% was found. Successful
469 integration was confirmed by amplification of the targeted region in the *asc* locus by PCR and
470 sequencing (SF4). Heterozygous *asc-EGFP/+* embryos were raised and incrossed to obtain
471 homozygous *asc-EGFP* embryos.

472 ***Chemical and inflammatory treatments***

473 *Caspase inhibition:* The pan-caspase inhibitor Q-VD-OPh hydrate (Sigma-Aldrich) was
474 resuspended in DMSO at a stock concentration of 10 mM. For caspase inhibition the compound
475 was added directly to the medium at a concentration of 100µM. *$CuSO_4$ treatment:* 3 dpf larvae
476 were treated with for 1h with Copper (II) sulphate (Sigma-Aldrich) at 25 µM. The compound was
477 washed off and specks were quantified 1 or 3 hours post-treatment.
478

479 **Acknowledgements:** We thank B. Bajoghli for helpful discussion and S. Kraus for technical
480 assistance. We are grateful to F. Peri for zebrafish hosting and J. N. Buffoni and C. Henkel for
481 caretaking, to M. Hammerschmidt for the sharing of the *Tg(krt19:dTomato-CAAX)* and
482 *Tg(krt4:GFP)* zebrafish lines and to D. Gilmour for the *Tg(βactin:NLS-tagBFP)* line generated by
483 L. Newton. We thank the EMBL Protein Expression and Purification Facility as well as the
484 EMBL Animal House for their role in generating the zebrafish ASC antibody, the EMBL
485 Advanced Light Microscopy Facility (ALMF) for continuous support and Zeiss for support of the
486 AMLF. We are grateful to D. Gilmour, A. Meijer and F. Peri for comments on this manuscript.
487 **Funding:** The laboratory of M.L. is supported by EMBO and EMBL. P.K. was supported by
488 Marie-Curie Initial Training Network FishForPharma; FP7-PEOPLE-2011-ITN, grant PITN-GA-
489 2011-289209. N.S. and Y.S. are supported by EMBL. The laboratory of J. W. is supported by
490 Heidelberg University and by the 7th framework program of the European Union (ERC advanced
491 grant GA 294354-ManISteC, J.W.). **Author contributions**: P.K. and M.L. designed the study.

492 P.K. generated the *Tg(HSE:asc-mKate2)*, *Tg(asc:asc-EGFP)* and *caspa* $^{-/-}$ lines and performed all
493 experiments except CLEM, which were performed with N.S. and Y.S. T.T. and J.W. contributed
494 with initial *Tg(asc:asc-EGFP)* design. P.K. and M.L. interpreted the data and wrote the paper. All
495 authors read and edited the manuscript. **Competing interests**: The authors declare no financial
496 conflict of interest.

497 **References**

498 1. P. Broz, V. M. Dixit, Inflammasomes: mechanism of assembly, regulation and signalling.
499 *Nat Rev Immunol*, 1–14 (2016).

500 2. D. Sharma, T.-D. Kanneganti, The cell biology of inflammasomes: Mechanisms of
501 inflammasome activation and regulation. *The Journal of Cell Biology*. **213**, 617–629
502 (2016).

503 3. A. V. Hauenstein, L. Zhang, H. Wu, The hierarchical structural architecture of
504 inflammasomes, supramolecular inflammatory machines. *Curr. Opin. Struct. Biol.* **31**, 75–
505 83 (2015).

506 4. S. M. Man, T.-D. Kanneganti, Converging roles of caspases in inflammasome activation,
507 cell death and innate immunity. *Nat Rev Immunol*. **16**, 7–21 (2015).

508 5. J. E. Vince, J. Silke, The intersection of cell death and inflammasome activation. *Cell. Mol.*
509 *Life Sci.* **73**, 2349–2367 (2016).

510 6. L. Vande Walle, M. Lamkanfi, Pyroptosis. *Curr Biol*. **26**, R568–72 (2016).

511 7. F. Hoss, J. F. Rodriguez-Alcazar, E. Latz, Assembly and regulation of ASC specks. *Cell.*
512 *Mol. Life Sci.*, 1–19 (2016).

513 8. E. de Alba, Structure and interdomain dynamics of apoptosis-associated speck-like protein
514 containing a CARD (ASC). *Journal of Biological Chemistry*. **284**, 32932–32941 (2009).

515 9. A. Lu *et al.*, Unified Polymerization Mechanism for the Assembly of ASC-Dependent
516 Inflammasomes. *Cell*. **156**, 1193–1206 (2014).

517 10. X. Cai *et al.*, Prion-like Polymerization Underlies Signal Transduction in Antiviral
518 Immune Defense and Inflammasome Activation. *Cell*. **156**, 1207–1222 (2014).

519 11. J. Masumoto *et al.*, ASC, a novel 22-kDa protein, aggregates during apoptosis of human
520 promyelocytic leukemia HL-60 cells. *J Biol Chem*. **274**, 33835–33838 (1999).

521 12. T. Fernandes-Alnemri *et al.*, The pyroptosome: a supramolecular assembly of ASC dimers
522 mediating inflammatory cell death via caspase-1 activation. *Cell Death Differ*. **14**, 1590–
523 1604 (2007).

524 13. J. C. Kagan, V. G. Magupalli, H. Wu, SMOCs: supramolecular organizing centres that
525 control innate immunity. *Nat Rev Immunol*. **14**, 821–826 (2014).

526 14. L. Sborgi *et al.*, Structure and assembly of the mouse ASC inflammasome by combined

527 NMR spectroscopy and cryo-electron microscopy. *Proceedings of the National Academy of*
528 *Sciences*. **112**, 13237–13242 (2015).

529 15. M. S. Dick, L. Sborgi, S. Rühl, S. Hiller, P. Broz, ASC filament formation serves as a
530 signal amplification mechanism for inflammasomes. *Nat Commun*. **7**, 11929 (2016).

531 16. F. I. Schmidt *et al.*, A single domain antibody fragment that recognizes the adaptor ASC
532 defines the role of ASC domains in inflammasome assembly. *J Exp Med*. **213**, 771–790
533 (2016).

534 17. J. Cheng *et al.*, Kinetic properties of ASC protein aggregation in epithelial cells. *J. Cell.*
535 *Physiol.* **222**, 738–747 (2010).

536 18. D. P. Sester *et al.*, A novel flow cytometric method to assess inflammasome formation. *The*
537 *Journal of Immunology*. **194**, 455–462 (2015).

538 19. A. Stutz, G. L. Horvath, B. G. Monks, E. Latz, ASC speck formation as a readout for
539 inflammasome activation. *Methods Mol Biol*. **1040**, 91–101 (2013).

540 20. M. Beilharz, D. De Nardo's, E. Latz, B. S. Franklin, Measuring NLR Oligomerization II:
541 Detection of ASC Speck Formation by Confocal Microscopy and Immunofluorescence.
542 *Methods Mol Biol*. **1417**, 145–158 (2016).

543 21. T.-C. Tzeng *et al.*, A Fluorescent Reporter Mouse for Inflammasome Assembly
544 Demonstrates an Important Role for Cell-Bound and Free ASC Specks during In Vivo
545 Infection. *CellReports*. **16**, 571–582 (2016).

546 22. A. S. Yazdi, S. K. Drexler, J. Tschopp, The Role of the Inflammasome in Nonmyeloid
547 Cells. *J. Clin. Immunol.* **30**, 623–627 (2010).

548 23. P. M. Peeters, E. F. Wouters, N. L. Reynaert, Immune Homeostasis in Epithelial Cells:
549 Evidence and Role of Inflammasome Signaling Reviewed. *Journal of Immunology*
550 *Research*. **2015**, 1–15 (2015).

551 24. P. Santana *et al.*, Is the inflammasome relevant for epithelial cell function? *Microbes*
552 *Infect.*, 1–9 (2015).

553 25. L. Feldmeyer, S. Werner, L. E. French, H.-D. Beer, Interleukin-1, inflammasomes and the
554 skin. *European Journal of Cell Biology*. **89**, 638–644 (2010).

555 26. S. K. Drexler *et al.*, Tissue-specific opposing functions of the inflammasome adaptor ASC
556 in the regulation of epithelial skin carcinogenesis. *Proceedings of the National Academy of*
557 *Sciences*. **109**, 18384–18389 (2012).

558 27. S. A. Renshaw, N. S. Trede, A model 450 million years in the making: zebrafish and
559 vertebrate immunity. *Dis Model Mech*. **5**, 38–47 (2012).

560 28. V. Torraca, S. Masud, H. P. Spaink, A. H. Meijer, Macrophage-pathogen interactions in
561 infectious diseases: new therapeutic insights from the zebrafish host model. *Dis Model*
562 *Mech*. **7**, 785–797 (2014).

563 29. M. van der Vaart, A. H. Meijer, H. P. Spaink, Pathogen Recognition and Activation of the
564 Innate Immune Response in Zebrafish. *Advances in Hematology*. **2012**, 1–19 (2012).

565 30. C.-Y. Lin, C.-Y. Chiang, H.-J. Tsai, Zebrafish and Medaka: new model organisms for
566 modern biomedical research. *Journal of Biomedical Science*, 1–11 (2016).

567 31. P. Kuri, K. Ellwanger, T. A. Kufer, M. Leptin, B. Bajoghli, A high-sensitivity, bi-
568 directional reporter to monitor NF-κB activity in cell culture and zebrafish in real-time. *J*
569 *Cell Sci* (2016), doi:10.1242/jcs.196485.

570 32. C. Stein, M. Caccamo, G. Laird, M. Leptin, Conservation and divergence of gene families
571 encoding components of innate immune response systems in zebrafish. *Genome Biol*. **8**,
572 R251 (2007).

573 33. J. D. Hansen, L. N. Vojtech, K. J. Laing, Sensing disease and danger: A survey of
574 vertebrate PRRs and their origins. *Dev Comp Immunol*. **35**, 886–897 (2011).

575 34. K. Howe *et al.*, Structure and evolutionary history of a large family of NLR proteins in the
576 zebrafish. *Open Biol*. **6**, 160009 (2016).

577 35. J. Masumoto *et al.*, Caspy, a zebrafish caspase, activated by ASC oligomerization is
578 required for pharyngeal arch development. *J Biol Chem*. **278**, 4268–4276 (2003).

579 36. J. Masumoto *et al.*, Expression of apoptosis-associated speck-like protein containing a
580 caspase recruitment domain, a pyrin N-terminal homology domain-containing protein, in
581 normal human tissues. *J. Histochem. Cytochem.* **49**, 1269–1275 (2001).

582 37. F. Peri, C. Nüsslein-Volhard, Live imaging of neuronal degradation by microglia reveals a
583 role for v0-ATPase a1 in phagosomal fusion in vivo. *Cell*. **133**, 916–927 (2008).

584 38. P. P. Hernandez *et al.*, Sublethal concentrations of waterborne copper induce cellular stress
585 and cell death in zebrafish embryos and larvae. *Biol. Res.* **44**, 7–15 (2011).

586 39. F. A. Olivari, P. P. Hernandez, M. L. Allende, Acute copper exposure induces oxidative
587 stress and cell death in lateral line hair cells of zebrafish larvae. *Brain Research*. **1244**, 1–
588 12 (2008).

589 40. C. A. d'Alençon *et al.*, A high-throughput chemically induced inflammation assay in
590 zebrafish. *BMC Biol.* **8**, 151 (2010).

591 41. B. Bajoghli, N. Aghaallaei, T. Heimbucher, T. Czerny, An artificial promoter construct for
592 heat-inducible misexpression during fish embryogenesis. *Dev Biol*. **271**, 416–430 (2004).

593 42. A. Lu, H. Wu, Structural mechanisms of inflammasome assembly. *FEBS Journal*. **282**,
594 435–444 (2015).

595 43. H. Hara *et al.*, Phosphorylation of the adaptor ASC acts as a molecular switch that controls
596 the formation of speck-like aggregates and inflammasome activity. *Nat Immunol*. **14**,
597 1247–1255 (2013).

598 44. Y.-C. Lin *et al.*, Syk is involved in NLRP3 inflammasome-mediated caspase-1 activation
599 through adaptor ASC phosphorylation and enhanced oligomerization. *Journal of Leukocyte*
600 *Biology*. **97**, 825–835 (2015).

601 45. I. Jorgensen, Y. Zhang, B. A. Krantz, E. A. Miao, Pyroptosis triggers pore-induced
602 intracellular traps (PITs) that capture bacteria and lead to their clearance by efferocytosis.

603 *Journal of Experimental Medicine*. **213**, 2113–2128 (2016).

604 46. A. Baroja-Mazo *et al.*, The NLRP3 inflammasome is released as a particulate danger signal
605 that amplifies the inflammatory response. *Nat Immunol*. **15**, 738–748 (2014).

606 47. B. S. Franklin *et al.*, The adaptor ASC has extracellular and "prionoid" activities that
607 propagate inflammation. *Nat Immunol*. **15**, 727–737 (2014).

608 48. L. N. Vojtech, N. Scharping, J. C. Woodson, J. D. Hansen, Roles of Inflammatory
609 Caspases during Processing of Zebrafish Interleukin-1β in Francisella noatunensis
610 Infection. *Infect Immun*. **80**, 2878–2885 (2012).

611 49. W. J. B. Vincent, C. M. Freisinger, P.-Y. Lam, A. Huttenlocher, J.-D. Sauer, Macrophages
612 mediate flagellin induced inflammasome activation and host defense in zebrafish. *Cellular*
613 *Microbiology*. **18**, 591–604 (2016).

614 50. M. Varela *et al.*, Cellular visualization of macrophage pyroptosis and interleukin-1β
615 release in a viral hemorrhagic infection in zebrafish larvae. *J Virol*. **88**, 12026–12040
616 (2014).

617 51. S. D. Tyrkalska *et al.*, Neutrophils mediate Salmonella Typhimurium clearance through the
618 GBP4 inflammasome-dependent production of prostaglandins. *Nat Commun*. **7**, 12077
619 (2016).

620 52. S. Rakers *et al.*, "Fish matters": the relevance of fish skin biology to investigative
621 dermatology. *Exp. Dermatol.* **19**, 313–324 (2010).

622 53. M. Pasparakis, I. Haase, F. O. Nestle, Mechanisms regulating skin immunity and
623 inflammation. *Nat Rev Immunol*. **14**, 289–301 (2014).

624 54. L. Feldmeyer *et al.*, The Inflammasome Mediates UVB-Induced Activation and Secretion
625 of Interleukin-1β by Keratinocytes. *Current Biology*. **17**, 1140–1145 (2007).

626 55. H. Watanabe *et al.*, Activation of the IL-1β-Processing Inflammasome Is Involved in
627 Contact Hypersensitivity. *J Investig Dermatol*. **127**, 1956–1963 (2007).

628 56. M. Reinholz *et al.*, HPV16 activates the AIM2 inflammasome in keratinocytes. *Arch*
629 *Dermatol Res*. **305**, 723–732 (2013).

630 57. X. Dai *et al.*, Mite allergen is a danger signal for the skin via activation of inflammasome
631 in keratinocytes. *J. Allergy Clin. Immunol.* **127**, 806–14.e1–4 (2011).

632 58. E. M. Weinheimer-Haus, R. E. Mirza, T. J. Koh, Nod-like receptor protein-3
633 inflammasome plays an important role during early stages of wound healing. *PLoS ONE*.
634 **10**, e0119106 (2015).

635 59. X. Cai, H. Xu, Z. J. Chen, Prion-Like Polymerization in Immunity and Inflammation. *Cold*
636 *Spring Harb Perspect Biol*, a023580 (2016).

637 60. B. Balci-Peynircioglu *et al.*, Expression of ASC in Renal Tissues of Familial
638 Mediterranean Fever Patients with Amyloidosis: Postulating a Role for ASC in AA Type
639 Amyloid Deposition. *Experimental Biology and Medicine*. **233**, 1324–1333 (2008).

640 61. P. Sagoo *et al.*, In vivo imaging of inflammasome activation reveals a subcapsular
641 macrophage burst response that mobilizes innate and adaptive immunity. *Nat Med*. **22**, 64–
642 71 (2016).

643 62. M. Stemmer, T. Thumberger, M. Del Sol Keyer, J. Wittbrodt, J. L. Mateo, CCTop: An
644 Intuitive, Flexible and Reliable CRISPR/Cas9 Target Prediction Tool. *PLoS ONE*. **10**,
645 e0124633 (2015).

646 63. W. Y. Hwang *et al.*, Efficient genome editing in zebrafish using a CRISPR-Cas system.
647 *Nat Biotechnol*. **31**, 227–229 (2013).

648 64. S. Kirchmaier, K. Lust, J. Wittbrodt, Golden GATEway cloning--a combinatorial approach
649 to generate fusion and recombination constructs. *PLoS ONE*. **8**, e76117 (2013).

650 65. Y. Hisano *et al.*, Precise in-frame integration of exogenous DNA mediated by
651 CRISPR/Cas9 system in zebrafish. *Sci Rep*. **5**, 8841 (2015).

652

653 **Figures and figure legends**

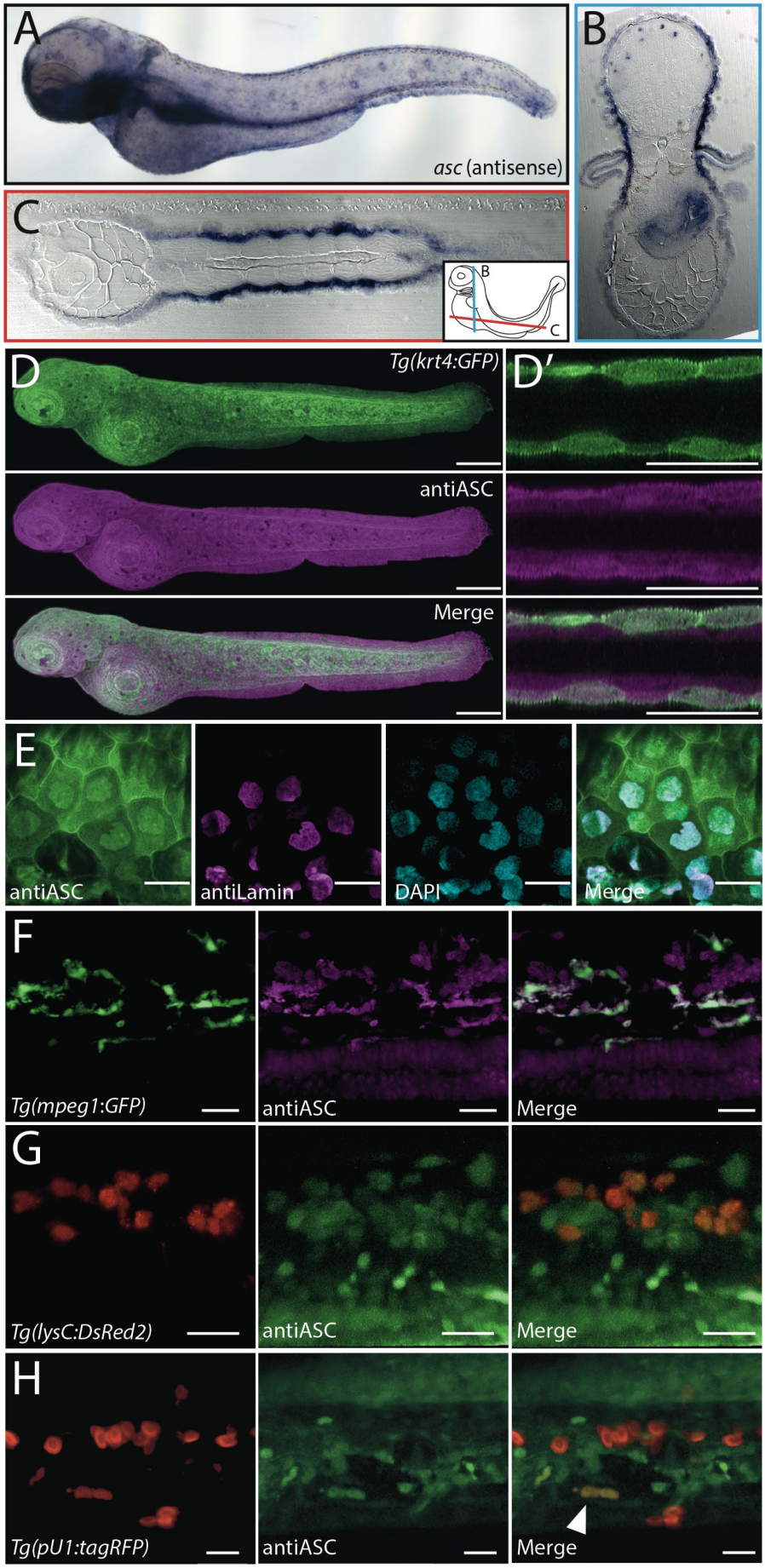
A
asc (antisense)
B
C
B
C
D
Tg(krt4:GFP)
D′
antiASC
Merge
E
antiASC
antiLamin
DAPI
Merge
F
Tg(mpeg1:GFP)
antiASC
Merge
G
Tg(lysC:DsRed2)
antiASC
Merge
H
Tg(pU1:tagRFP)
antiASC
Merge

654 **Fig. 1. *asc* is expressed during zebrafish early development.** *asc* whole-mount *in situ*
655 hybridization (*wish*) of 3 dpf zebrafish larvae [A] with cross [B] and longitudinal [C] sectioning
656 of plastic embedded *wish* sample showing expression in epidermis, intestinal epithelium, and
657 cells located in the brain. Immunostaining of ASC in 3dpf *Tg(krt4:GFP)* larva [D]. Optical cross
658 section of lateral fin showing GFP expression in the enveloping layer (EVL), and ASC expression
659 on both epidermal layers [D'']. Wildtype 3 dpf larva immunostained for ASC, together with
660 nuclear envelope marker Lamin and DAPI shows its nuclear and cytoplasmic localization [E].
661 Immunostaining of 3 dpf *Tg(mpeg:GFP)* [F], *Tg(lysC:DsRed2)* [G] and *Tg(pU1:tagRFP)* [H]
662 larvae showing expression of ASC in macrophages, neutrophils, and a single myeloid cell in the
663 CHT [H, white arrowhead]. Scale bars, 300 μm for full larvae, otherwise 30 μm.

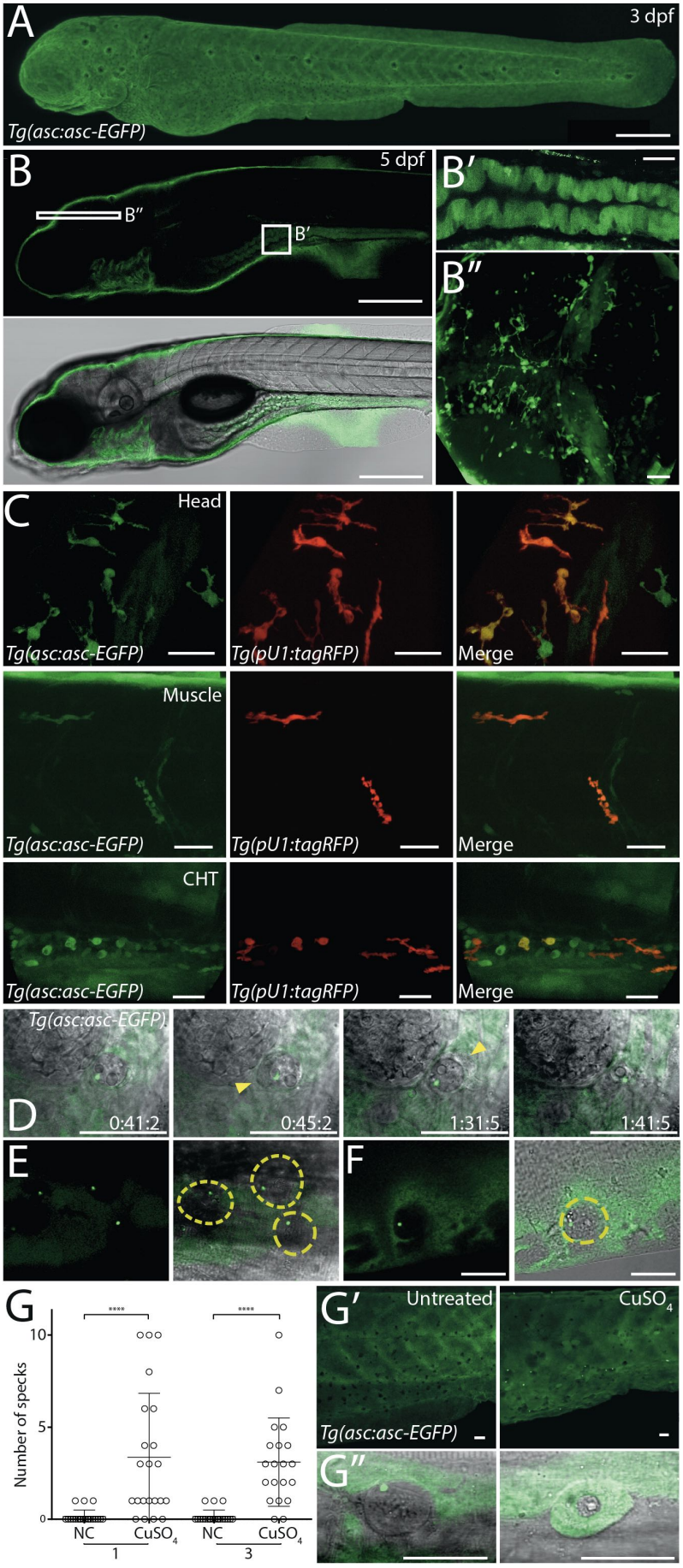
A
3 dpf
Tg(asc:asc-EGFP)
B
5 dpf
B″
B′
B′
B″
C
Head
Tg(asc:asc-EGFP)
Tg(pU1:tagRFP)
Merge
Muscle
Tg(asc:asc-EGFP)
Tg(pU1:tagRFP)
Merge
CHT
Tg(asc:asc-EGFP)
Tg(pU1:tagRFP)
Merge
Tg(asc:asc-EGFP)
D
0:41:2
0:45:2
1:31:5
1:41:5
E
F
G
Number of specks
10
5
0
****
****
NC
CuSO4
NC
CuSO4
1
3
G′
Untreated
CuSO4
Tg(asc:asc-EGFP)
G″

664 **Fig. 2. Endogenous ASC forms specks *in vivo* in the *Tg(asc:asc-EGFP)* line.** Live imaging of
665 *Tg(asc:asc-EGFP)* 3 dpf [A] and 5 dpf [B] larvae, with intestine [B'] and head [B''] optical
666 sections. Live imaging of head, muscle and caudal hematopoietic tissue (CHT) of 3 dpf
667 *Tg(asc:asc-EGFP, pU1:tagRFP*) larvae [C]. Time lapse imaging of keratinocyte with speck.
668 Single plane merged with the brightfield is shown. Yellow arrowheads highlight a second cell that
669 appears to surround the speck-containing cell [D]. Live imaging of specks in the dorsal epidermis
670 [E] and ventral fin [F] of 3 dpf Tg(*asc:asc-EGFP*) larvae. Merge with brightfield plane shows
671 each speck is within a cell with altered morphology (dashed yellow line). *Tg(asc:asc-EGFP)* 3
672 dpf larvae were treated with 25 μM $CuSO_4$ for 1h. At 1 and 3 hours post treatment (hpt) number
673 of specks per larva were quantified (One way ANOVA, ****P<0.0001) [G]. Live imaging of
674 untreated and treated larvae showing high damage of epidermis and increase in specks [G'],
675 examples in treated embryo of single cells displaying altered morphology with and without speck
676 formation [G''']. Scale bars, 300 μm for full larvae, otherwise 30 μm.

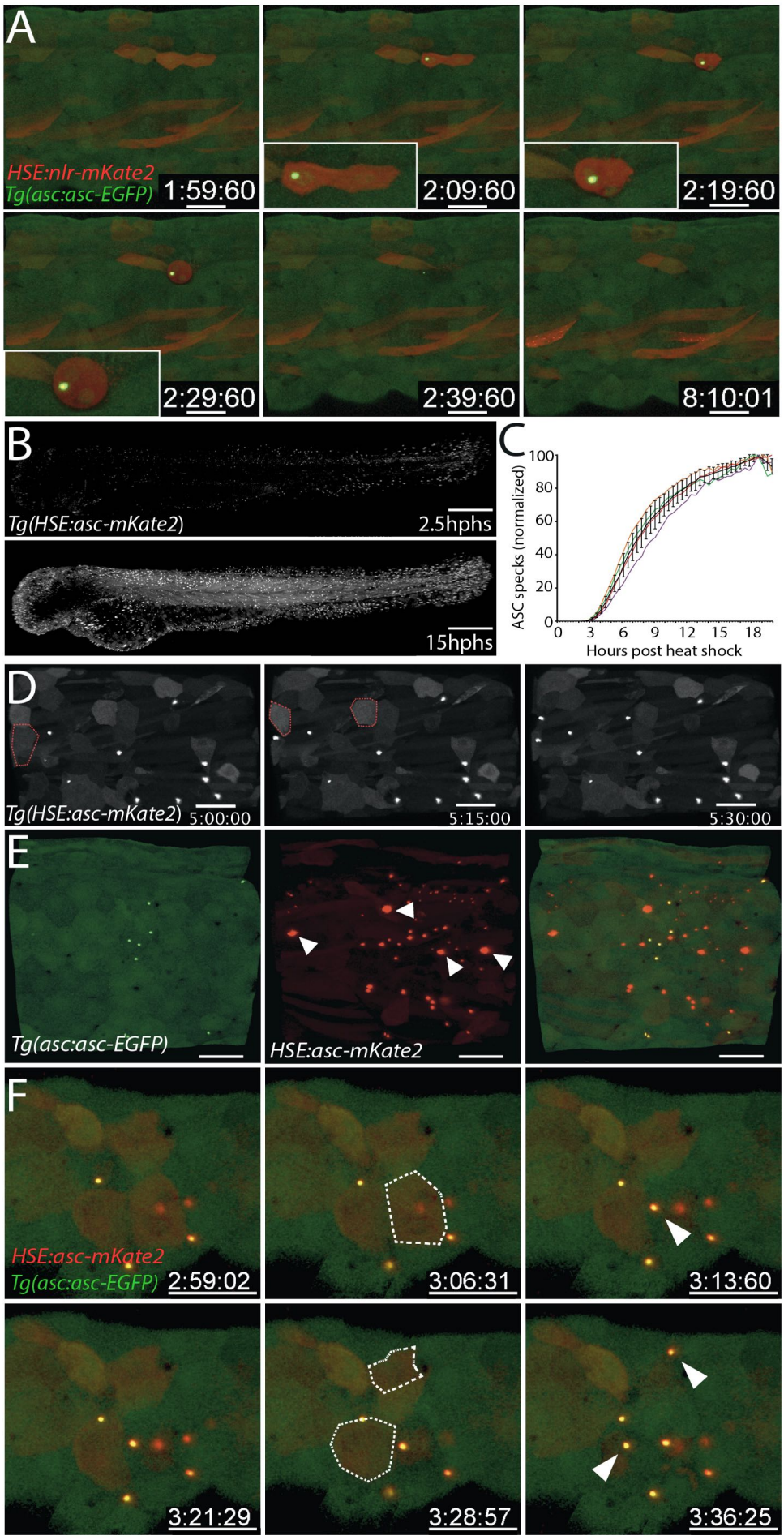
A
HSE:nlr-mKate2
Tg(asc:asc-EGFP)
1:59:60
2:09:60
2:19:60
2:29:60
2:39:60
8:10:01
B
Tg(HSE:asc-mKate2)
2.5hphs
15hphs
C
ASC specks (normalized)
100
80
60
40
20
0
0 3 6 9 12 15 18
Hours post heat shock
D
Tg(HSE:asc-mKate2)
5:00:00
5:15:00
5:30:00
E
Tg(asc:asc-EGFP)
HSE:asc-mKate2
F
HSE:asc-mKate2
Tg(asc:asc-EGFP)
2:59:02
3:06:31
3:13:60
3:21:29
3:28:57
3:36:25

677 **Fig. 3. Expression of *asc* or *nlr* induces speck formation.** Timelapse imaging of trunk from 3
678 dpf *Tg(asc:asc-gfp)* larva transiently expressing *HSE:nlr-mKate2* at 7 hphs. Inlet shows enlarged
679 view of NLR-mkate2-expressing keratinocytes after speck formation [A]. Time lapse imaging of
680 3 dpf *Tg(HSE:asc-mKate2)* embryos after heat shock. Shown are timepoints corresponding to 2.5
681 hphs (upper panel) and 15 hphs (lower panel) [B]. Quantification of speck numbers over entire
682 larvae after heat shock using 3D image analysis software [C]. Time lapse of 3 dpf *Tg(HSE:asc-*
683 *mKate2)* larvae 3 hphs showing recruitment of ASC-mKate to a single speck per cell (demarcated
684 by dashed red line in timepoint before speck formation). [D]. Live imaging of *Tg(asc:asc-gfp)*
685 transiently expressing *HSE:asc-mKate2* 13 hphs [E]. White arrowheads show specks assembled
686 in muscles. Time lapse imaging of *Tg(asc:asc-gfp)* larva transiently expressing *HSE:asc-mKate2*.
687 Individual keratinocytes are demarcated with a dashed white line at the time point before the
688 formation of ASC-mKate2 and ASC-GFP double positive specks (white arrowheads). Time lapse
689 was started 3.5 hphs [D]. Single time point of trunk *Tg(asc:asc-gfp)* transiently expressing ASC-
690 mKate2. Scale bars, 300 µm for full larvae, otherwise 40 µm.

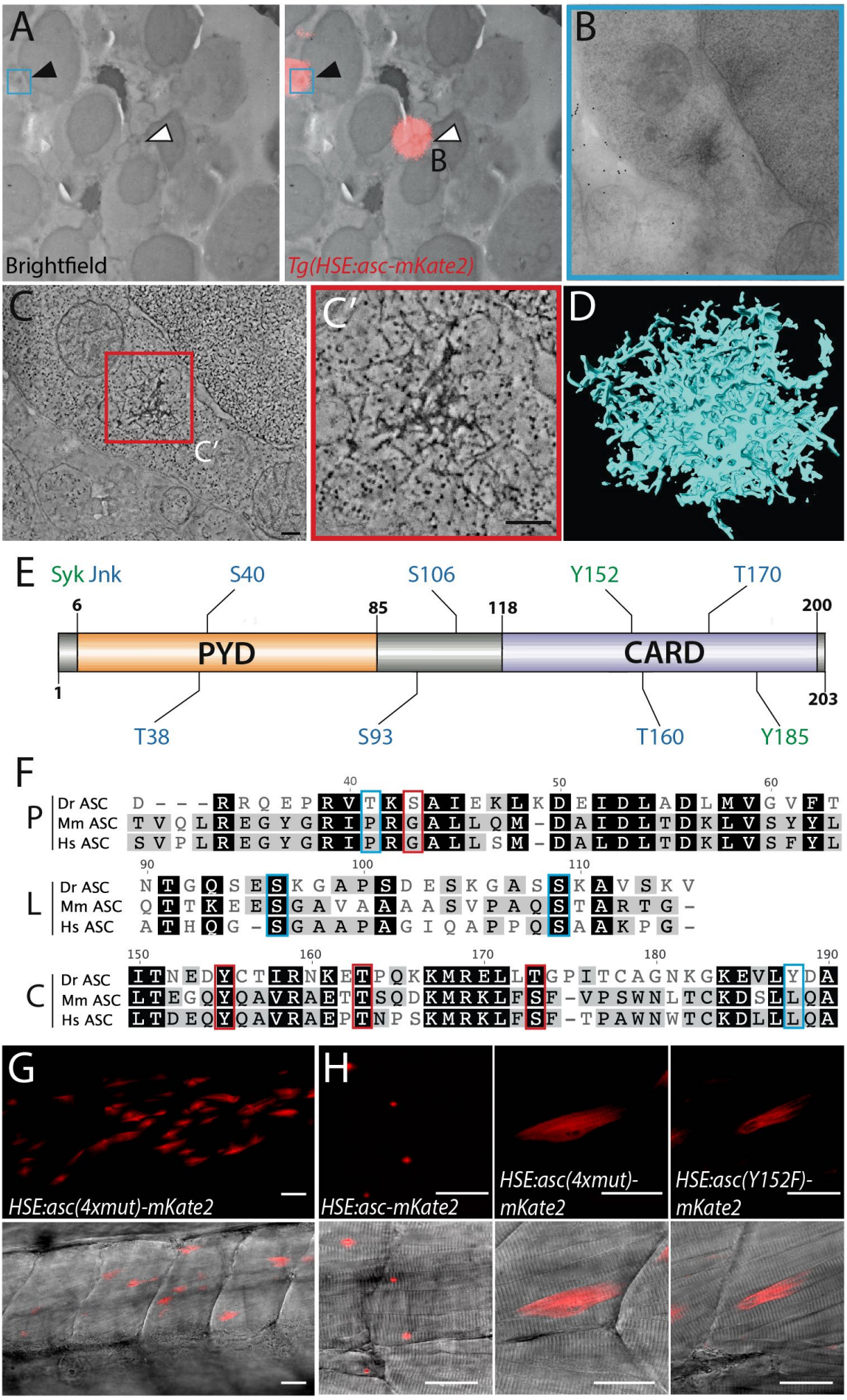
A
Brightfield
Tg(HSE:asc-mKate2)
B
C
C′
D
E
Syk Jnk
S40
S106
Y152
T170
6
85
118
200
PYD
CARD
1
203
T38
S93
T160
Y185
F
P
Dr ASC
Mm ASC
Hs ASC
L
C
G
HSE:asc(4xmut)-mKate2
H
HSE:asc-mKate2
HSE:asc(4xmut)-mKate2
HSE:asc(Y152F)-mKate2

691 **Fig. 4. ASC specks are highly intercrossed filamentous structures whose clustering is altered**
692 **by point mutations.** Correlative Light Electron Microscopy (CLEM) of high-pressure frozen 3
693 dpf *Tg(HSE:asc-mKate2)* larvae 18 hphs [A-D]. Low magnification electron micrograph [A, left
694 panel] and overlay with red channel [A, right panel] imaged with light microscope. White and
695 black arrowheads show location of specks. Area of interest (blue) imaged with electron
696 microscope [B]. TEM tomography slice of speck (black arrowhead) [C] and an enlarged view of
697 intercrossed filaments [C'']. 3D reconstruction of speck after manual tracking of individual
698 filaments [D]. Scale bars, 200 nm. Results from phosphorylation sites analysis using the online
699 tool GPS 2.1.1 depicting Syk and Jnk-specific predicted phosphorylation sites in zebrafish ASC
700 [E]. Portions of zebrafish (Dr), mouse (Mm) and human (Hs) ASC protein alignment separated by
701 domain (P, PYD; L, linker; C, CARD). Aminoacids identified in the analysis are boxed, in red
702 those mutagenized [F]. Live imaging of larvae transiently expressing *HSE:asc(4xmut)-mKate2*,
703 containing 4 missense mutations (T38A, Y152F, T160A and T170A) [G]. Single muscle cell in
704 larvae transiently expressing either *HSE:asc-mKate2* or, *HSE:asc(4xmut)-mKate2* or
705 *HSE:asc(Y152F)-mKate2* [H]. Scale bars, 30 µm.

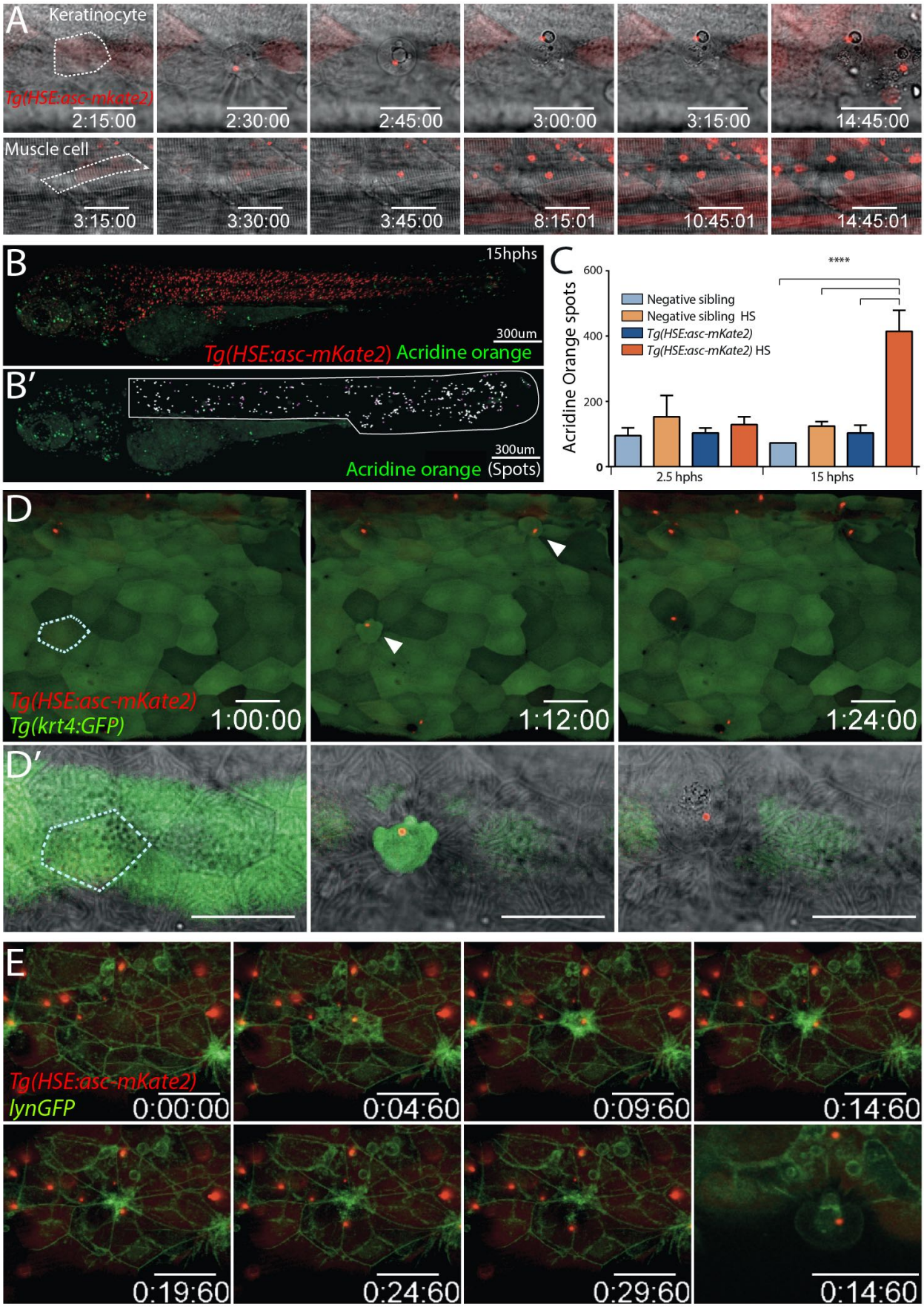

706 **Fig. 5. ASC speck formation in keratinocytes leads to cell death.** Time lapse imaging of speck
707 formation in keratinocyte (top) and muscle cell (bottom) in 3 dpf *Tg(HSE:asc-mKate2)* larva 3

708 hphs. Drastic morphological changes occur only in keratinocytes [A]. *Tg(HSE:asc-mKate2)*
709 larvae and negative siblings were stained with acridine orange and imaged 2.5 and 15 hphs [B,
710 upper panel]. 3D rendering of individual larvae manually segmented to exclude the head, heart
711 and yolk regions. Acridine orange spots in segmented region were quantified using 3D image
712 analysis software [white spots, B']. Spots positive in the red channel were excluded [magenta
713 spots, B']. Histogram of acridine orange spots in each group shows only transgenic larvae 15
714 hphs have significantly higher cell death (One way ANOVA, ****P<0.0001) [C]. Time lapse
715 imaging of *Tg(HSE:asc-mKate2, krt4:GFP)* larvae 3 hphs showing morphological changes in
716 EVL keratinocyte upon speck formation [white arrowheads, D, upper row]. Enlarged view of
717 EVL keratinocyte [dashed white outline, D] of single plane with the brightfield [D']. Time lapse
718 imaging of *Tg(HSE:asc-mKate2)* injected with *lynGFP* mRNA for membrane visualization 8
719 hphs. Epidermal layer shows extrusion and gap closure after speck formation [E]. Single plane
720 showing extruded keratinocyte [E']. Scale bars, 30 µm.

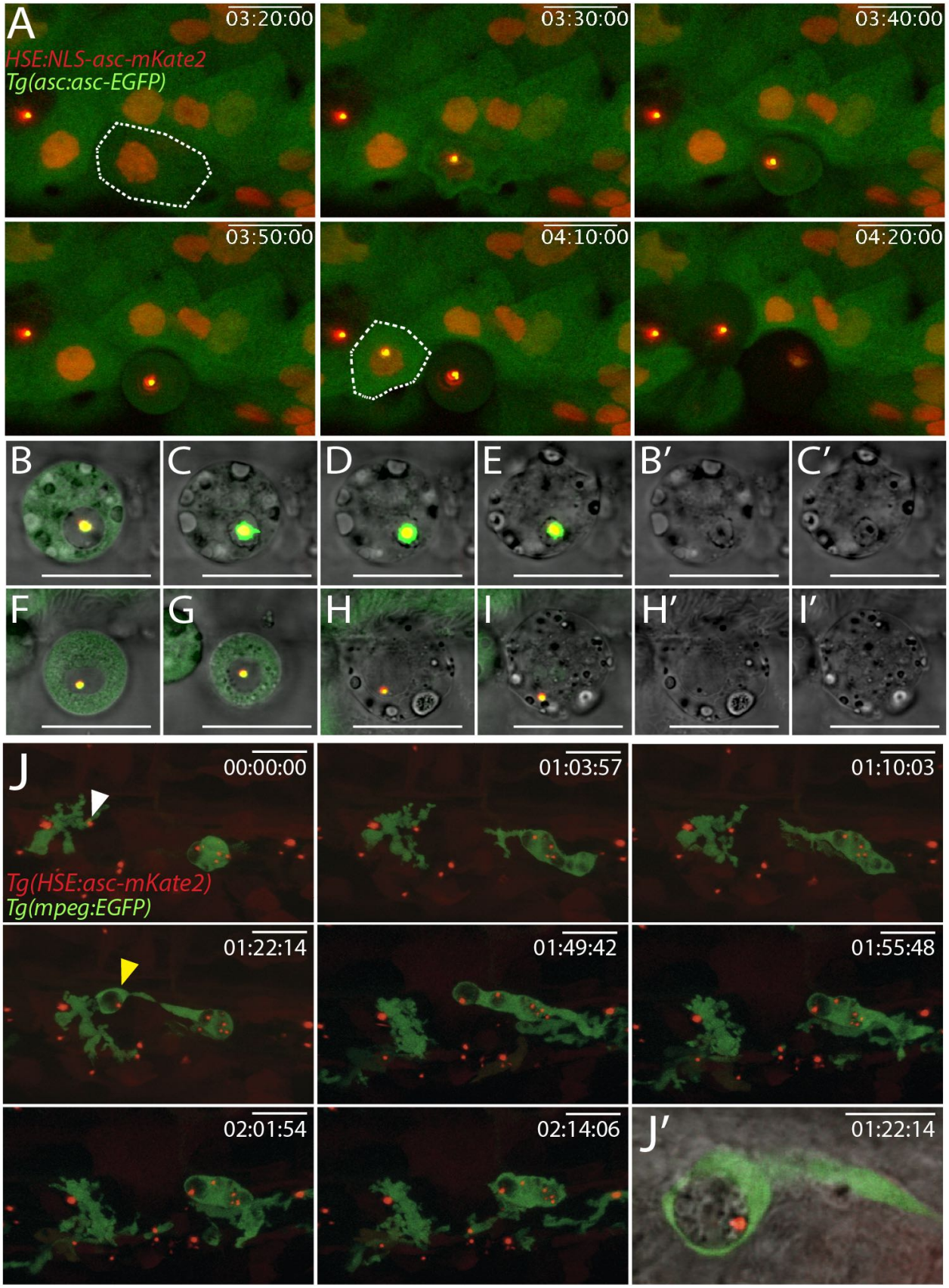

721 **Fig. 6. Nuclear specks causing cell death and macrophage engulfment of speck-containing**
722 **cellular debris.** Time lapse of 3 dpf *Tg(asc:asc-EGFP)* larvae transiently expressing *HSE:NLS-*
723 *asc-mKate2* 6 hphs, showing nuclear speck assembly in keratinocytes (white dashed line) leads to

724 cell death [A]. Cell undergoing cell death with nuclear speck and without depletion of ASC-GFP
725 in the cytoplasm [B-E]. Brightfield of respective timepoints show breakdown of nuclear envelope
726 allows recruitment of cytoplasmic ASC-GFP [B' and C']. Loss of plasma membrane integrity [F-
727 I] prior to nuclear envelope breakdown, results in leakage of cytoplasmic ASC-GFP as shown in
728 brightfield [H' and I']. Time lapse imaging of *Tg(HSE:asc-mKate2, mpeg:EGFP)* larva 17 hphs
729 shows macrophage engulfing a speck (white arrowhead) [J]. Brightfield merge of single plane
730 showing phagocytic cup (yellow arrowhead) [J']. Scale bars, 20 μm.

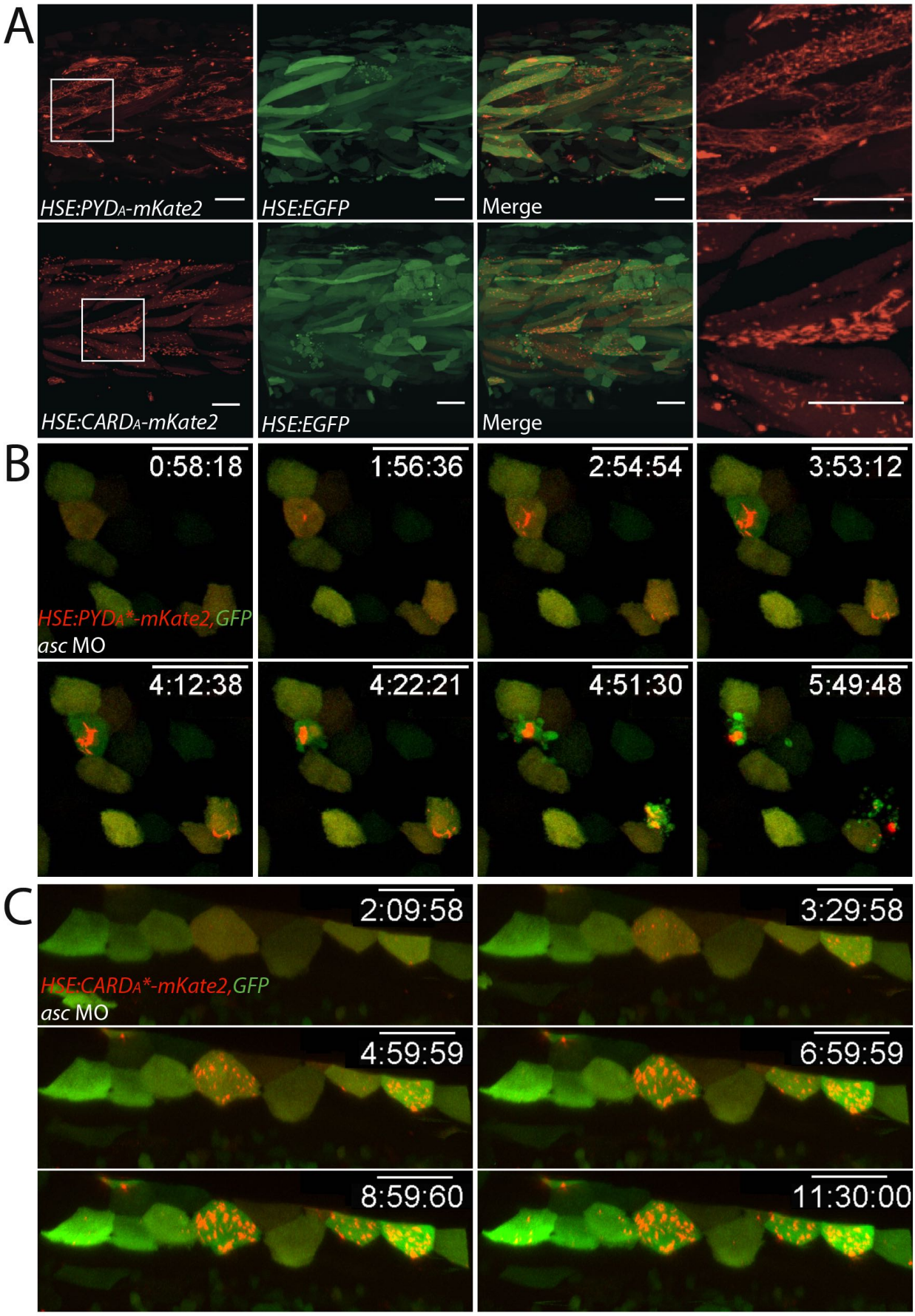

731 **Fig. 7. PYD aggregates lead to delayed pyroptosis.** Live imaging of 3 dpf larvae transiently
732 expressed *HSE:PYD$_A$-mKate2* or *HSE:CARD$_A$-mKate2* with GFP 17 hphs [A]. Expression of

733 either domain leads to the formation of filamentous aggregates of varying lengths in muscle cells.
734 Time lapse imaging of *asc* morpholino-injected *Tg(asc:asc-EGFP)* larvae transiently expressing
735 the *asc* morpholino resistant *HSE:PYD*$_A$-mKate2* [B] or *HSE:CARD$_A$-mKate2* [C] with GFP. If
736 endogenous ASC is absent, PYD$_A$ aggregates cause cell death 2 hours after the aggregates first
737 form, whereas CARD$_A$ aggregates do not, even 10 hours after their assembly. Scale bars, 40 µm.

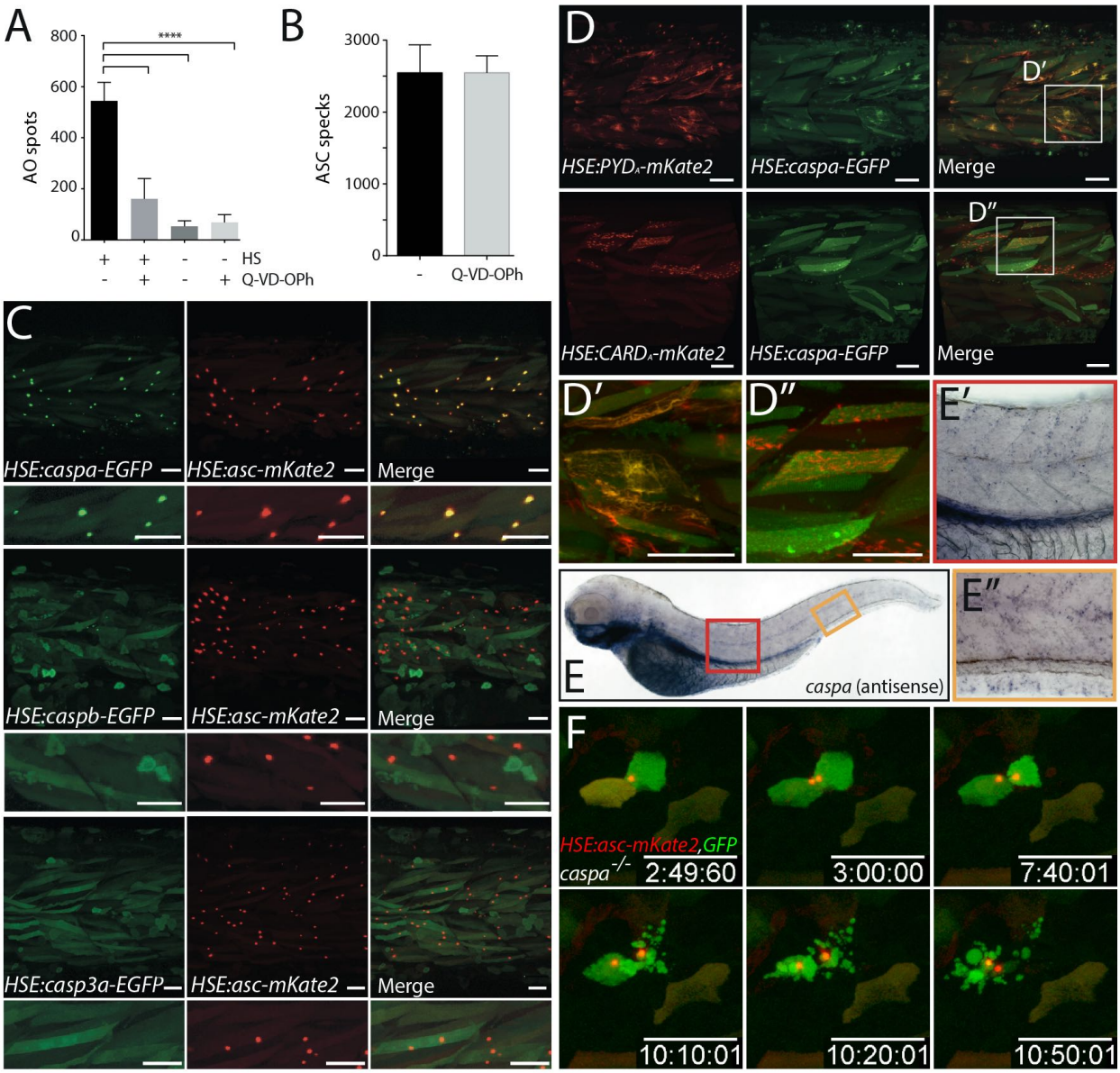

738 **Fig. 8. ASC speck formation leads to pyroptosis via activation of Caspa through PYD-PYD**
739 **domain interaction.** 3 dpf *Tg(HSE:asc-mKate2)* larvae treated with the pan-caspase inhibitor Q-
740 VD-Oph (100 µM) after or without heat shock were stained with acridine orange at 17 hphs.
741 Acridine orange spots [A] and specks [B] were quantified. Treatment with Q-VD-Oph
742 significantly diminished cell death caused by speck formation compared to non-treated controls
743 (One way ANOVA, *****P*<0.0001). Live imaging of transient expression of *HSE:caspa-EGFP*,
744 *HSE:caspb-EGFP* or *HSE:casp3a-EGFP* with *HSE:asc-mKate2* [C]. Recruitment to the ASC-

745 mKate2 specks only occurs in the case of Caspa-GFP coexpression. Live imaging of heat-shock
746 induced transient expression of *HSE:PYD$_A$-mKate2* or *HSE:CARD$_A$-mKate2* with *HSE:caspa-*
747 *EGFP* in 3 dpf larvae 19 hphs [D] with enlarged view of single cells [D' and D"]. PYD$_A$, but not
748 CARD$_A$, aggregates recruit Caspa-GFP. *caspa* antisense *wish* in 3 dpf larvae [E]. Enlarged view
749 shows expression in skin and ventral fin [E' and E"]. Time lapse imaging of *caspa* mutants
750 transiently expressing *HSE:asc-mKate2* with GFP 3 hphs [F]. Cell death response is severely
751 affected in *caspa*$^{-/-}$ keratinocytes, with cells dying an apoptotic-like death more than 7 hours after
752 speck formation. Scale bars, 40 μm.

753

754

755 **Supplemental Information**

756 **Supplemental Experimental Procedures**

757 ***Zebrafish care, transgenic lines and genotyping***

758 Zebrafish (*Danio rerio*) were cared for as described previously (*1*). The chemical 1-phenyl-2-
759 thiourea (PTU, Sigma-Aldrich) was added to E3 medium at a concentration of 0.2 mM to inhibit
760 pigmentation. The Tupfel Long Fin (TLF) strain was used as wild type. The following transgenic
761 lines were used: *mpeg1:EGFP* (*2*), *pu1:Gal4-UAS-TagRFP* (*3*), *lysC:DsRed2* (*4*), *βactin:NLS-*
762 *tagBFP* (Lionel Newton, unpublished), *krt4:GFP* and *krt19:Tomato-CAAX* (*5*). Lines generated
763 in this study are described below. gDNA was extracted from full larvae or adult fin clips using the
764 QuickExtract DNA Extraction Solution (Epicentre), genotyping was carried out with Phusion
765 High-Fidelity DNA Polymerase (Thermo Fisher Scientific). All animal experiments described in
766 the present study were conducted under the rules of the European Molecular Biology Laboratory
767 and the guidelines of the European Commission, Directive 2010/63/EU.

768 ***Acridine orange staining***

769 Acridine orange is a live dye that has previously been used to label dying cells in live zebrafish
770 embryos (*6*). Larvae were stained by immersion for 45 min in a 1:1500 dilution of a 10mg/ml
771 stock (Sigma-Aldrich) prepared in E3, rinsed to remove excess dye, anesthetized, mounted and
772 imaged directly afterwards. Because the dye is light-sensitive, larvae were kept in the dark during
773 staining.

774 ***Cloning of expression vectors and expression induction***

775 All expression vectors were coinjected with transposase mRNA (100 ng/µl) in embryos at one-
776 cell stage. For all heat shock-driven expression, the fusion protein of interest was cloned into a
777 vector backbone containing a bidirectional heat shock element (HSE) as promoter (*7*), Tol2 sites
778 for transgenesis and carrying the *cmlc2:tagRFP* as a transgenic marker (*8*). To induce expression,
779 injected embryos with red "bleeding heart" expression were heat-shocked at 39 °C in a heating
780 block at any stage between 2.5 dpf and 3.5 dpf. The transgenic *HSE:asc-mKate2* line was
781 generated by raising embryos (F0) carrying the heart marker without exposing them to heat-
782 shock. The *ubi:LexPR,LexOP:asc-mKate2* vector containing the LexPR/LexOP transactivation
783 system (*9*) was generated via Gateway recombination cloning (Thermo Fisher Scientific) of
784 *ubi*(p5E)/*LexPR,LexOP*(pME)/*asc-mKate2*(p3E). Expression was induced upon addition of 10
785 µM Mifepristone (RU486, Sigma-Aldrich).

786 ***Site-directed mutagenesis***

787 For site-directed mutagenesis of the *HSE:asc-mKate2* the QuikChange II XL Site-Directed
788 Mutagenesis Kit (Agilent Technologies) was used according to manufacturer's instructions. To
789 make *HSE:asc-mKate2 asc* ATG morpholino-resistant a total of 6 bp changes were made with
790 two rounds of site-directed mutagenesis, the first introduced the G6A, A9G, T12A mutations with
791 one complementary primer pair
792 (GCTTGAATTCACCATGGCAGAGTCATTCAAGGAGCAGCTGCAG) and the second
793 introduced the G18A, G21A, G24A mutations
794 (CTCAAAAGCCTCCTGCAGTTGTTCTTTGAATGACTCTGCCATGGTG). Specific primer
795 pairs were used to mutate each phosphorylation site: T38A
796 (GGAGGCAGGAACCGCGCGTCGCAAAGTCTGCAATCGAAAAGCTG), Y152F
797 (CATCACAAATGAGGATTTCTGTACCATTCGTAATAAG), T160A
798 (CCATTCGTAATAAGGAGGCTCCTCAAAAGAAGATG), T170A
799 (GAGAGAGTTATTAGCAGGCCCAATCACATG).

800 ***sgRNA and mRNA synthesis***

801 To synthesize the templates for sgRNAs targeting *caspa*, the two-oligo PCR method (*10*) was
802 used. For sgRNAs targeting *asc*, sgRNA-containing plasmids were cloned using oligo annealing
803 (*11*). All sgRNAs were transcribed using the MEGAshortscript T7 Transcription Kit (Ambion).
804 To synthesize mRNA, linearized pCS2 + DNA vector containing the gene of interest was used as
805 template and transcribed with the mMessage mMachine SP6 Transcription Kit (Ambion). RNA
806 from *in vitro* transcriptions was purified with the RNA Clean & Concentrator-5 (Zymo Research).
807 mRNAs were injected into one-cell stage embryos.

808 ***RNA extraction, cDNA synthesis and RT-PCR***

809 Total RNA was extracted from larvae using TriFast (Peqlab) according to manufacturer's
810 instructions. To prevent contamination from gDNA, samples were treated with RQ1 RNase-Free
811 DNase (Promega) and then repurified using TriFast. To generate first strand cDNA from total
812 extracted RNA was generated using the Superscript III Reverse Transcriptase enzyme
813 (Invitrogen). The obtained cDNA was directly used for reverse transcription PCR using Phusion
814 High-Fidelity DNA Polymerase (Thermo Fisher Scientific). The following primers were used:
815 *asc* (Fwd: AGTAGCAGATGATCTATTGAGG, Rev:
816 AGAGCATCATACAAGACTTCTTTCC), *caspa* (Fwd:

817 CAGTCAGCGCCCTGAGCTAAACATG, Rev: TCAACTGAGCTGGATCCTTCGG), *ef1a*
818 (Fwd: CTTCTCAGGCTGACTGTGC, Rev: CCGCTAGCATTACCCTCC).

819 ***Whole-mount in situ hybridization, plastic embedding and sectioning***

820 *In situ* hybridization was performed essentially as described previously (*12*). Antisense and sense
821 probes for *asc* and *caspa* CDS were transcribed *in vitro* from linearized pCS2 + DNA vector
822 containing the entire CDS of each gene by use of the DIG RNA Labeling Kit (Roche) and
823 purified SigmaSpin Post-Reaction Clean-Up Columns (Sigma-Aldrich). BM Purple AP substrate
824 (Roche) was used for staining. Whole-mount *in situ* samples were sectioned using the Leica
825 Historesin embedding kit (Leica Microsystems) according to manufacturer's instructions.
826 Sectioning was carried out manually using Leica RM2235 Manual Rotary Microtome (Leica
827 Microsystems).

828 ***ASC polyclonal antibody production***

829 ASC polyclonal antibody was generated from the full-length recombinant ASC purified from a
830 bacterial expression system. Antigen production and antibody purification were carried out by the
831 Protein Expression and Purification Core Facility at EMBL. The rabbit immunization procedure
832 and all animal handling were performed by the Polyclonal Antibody service at the EMBL
833 Laboratory Animal Resources. Antibody specificity was confirmed by using preimmunization
834 serum as a negative control and in the immunostaining pattern in *asc* morphant embryos.

835 ***Immunostaining***

836 Two variants of immunostainings were used, depending on the tissue of interest.
837 Immunostainings of myeloid cells were carried out as previously described (*13*). To visualize
838 keratinocyte stainings, a less abrasive protocol lacking methanol dehydration, proteinase K
839 treatment and postfixation steps, was used for epidermis preservation. The following primary
840 antibodies were used antiASC (1:10^3 dilution), antiGFP (Santa Cruz, 1:10^4 dilution) or antiLamin
841 B2 (1:200 dilution, Thermo Fisher Scientific). Secondary antibodies (Invitrogen) were coupled to
842 Alexa-488, -568 and -647 (1:500, 1:500, 1:300 dilutions, respectively).

843 ***Protein extraction and western blotting***

844 To obtain whole-embryo protein lysate, embryos were sonicated in fresh buffer (10 mM HEPES
845 pH 7.5, 100 mM KCl, 2 mM $MgCl_2$, 0.1 mM $CaCl_2$, 5 mM EGTA pH 8.0, 1 mM NaF, 1 mM
846 Na_3VO_4, 0.5% Triton, Protease inhibitor cocktail tablets [1 tablet/10 ml, Roche]). Lysate was
847 cleared by centrifugation and supernatant was collected and stored after addition of 5xSDS

848 Sample Buffer (10% SDS, 20% glycerol, 0.2 M Tris-HCl pH 6.8, 0.05% Bromophenol Blue and
849 10% β-mercaptoethanol added right before use). Prepared protein samples were separated by
850 SDS-PAGE using the Mini-PROTEAN Vertical Electrophoresis Cell system (Bio-Rad),
851 transferred to a polyvinylidene difluoride (PVDF) membrane (Immobilion-P) in a semi-dry
852 transfer cell (Bio-Rad) and probed using antiASC (1:10^3 or 1:10^4 dilution) or antiGFP (Santa
853 Cruz, 1:10^4 dilution) and developed with corresponding HRP-coupled secondary antibodies
854 (Jackson ImmunoResearch). Detection was carried out using Luminata Crescendo Western HRP
855 Substrate (Millipore).

856 ***Generation of caspa mutant***

857 *sgRNA design:* Small guide RNAs (sgRNAs) targeting the first exon of zebrafish gene *caspa*
858 (ENSDARG00000008165) were designed using the tool at http://crispr.mit.edu (*14*) and selected
859 as reported (*10*). *sgRNA in vivo validation:* To test whether sgRNAs were targeting the region of
860 interest *in vivo*, sgRNAs were injected in varying concentrations (120-275 ng/µl) together with 1
861 µl of in-house (Protein Expression and Purification facility, EMBL Heidelberg) synthesized Cas9
862 protein (4 mg/ml) complemented with ca. 150 mM KCl into fertilized eggs at the one-cell stage of
863 the zebrafish TLF strain. Successful knockdown was verified by sequencing of an 800 bp PCR
864 product from the targeted region of *caspa* (Fwd: TGGGTTAACTAGGCAAGTCAGGG, Rev:
865 AGGGTGTATCAGGACTTGGGCCC or Rev: CCACACATGGGAGGTGTGAA). *Screening:*
866 Embryos injected with the most efficient sgRNA (GGACGCTTTAAGTAATATTGGGG) were
867 raised to adulthood to obtain the F0. At 6 wpf, F0 fish were genotyped by fin clipping. F0 fish
868 showing successful targeting were incrossed and the F1 generation was raised to adulthood.
869 Through genotyping of the F1 adults, two KO alleles were found: the *caspa*^{K**} allele carrying a
870 5'-AAATAATAA -3' insertion at the expected Cas9 cleavage site resulting in two STOP codons
871 and the *caspa*$^{\Delta 800}$, carrying a deletion of ca. 800 bp including most of the first exon and part of the
872 first intron that resulted in a nonsense mutation. Heterozygous F1 fish carrying both alleles were
873 incrossed to obtain homozygous mutants with either the *caspa*^{K**} or the *caspa*$^{\Delta 800}$ deletion allele.

874 ***CLEM***

875 For CLEM analysis, the embryos were high-pressure frozen (HPM010 AbraFluid), using 20%
876 dextran or 20% ficoll as cryoprotectant. The embryos were pierced with a needle in a cryo-
877 microtome chamber (Leica EM FC6) at -160˚C to facilitate freeze substitution (*15*). Embryos
878 were then freeze-substituted (EM-AFS2, Leica Microsystems) with 0.1% Uranyl Acetate (UA) in
879 acetone at -90˚C for 48 hours. The temperature was then raised to -45˚C at 3.5˚C/h and samples
880 were further incubated for 5 hours. After rinsing in acetone, the samples were infiltrated in

881 Lowicryl HM20 resin, while raising the temperature to -25˚C and left to polymerize under UV
882 light for 48 hours at -25°C and for further 9 hours while the temperature was gradually raised to
883 20˚C (5˚C/h). Thick sections (300 nm) were cut from the polymerized resin block and picked up
884 on carbon coated mesh grids. The imaging of sections by fluorescence microscopy (FM) was
885 carried out as previously described (*16*, *17*)using a widefield fluorescence microscope (Nikon Ti-
886 E). Images were collected with mCherry-specific settings as well as transmitted light.
887 TEM tomography was acquired with a FEI Tecnai F30 electron microscope. Dual-axis
888 tomograms were obtained using SerialEM (*18*) and reconstructed in eTomo, part of the IMOD
889 software package (*19*)(Boulder Laboratory, University of Colorado). Correlation between light
890 and electron micrographs was carried out with the plugin ec-CLEM
891 (http://icy.bioimageanalysis.org/plugin/ec-CLEM) of the software platform Icy (*20*). Features
892 visible in both the light and electron microscopy images were manually assigned by clicking. The
893 coordinates of pairs in the two imaging modalities were used to calculate a linear transformation,
894 which allowed to map the coordinates of the fluorescent spot of interest (red channel) and to
895 overlay it on the electron micrograph. The tomograms were threshold segmented with the
896 Microscopy Image Browser platform (*21*), the resulting model was loaded into the digital space
897 of Amira for visualisation (FEI Company, Hillsboro, Oregon).

898 ***Software***

899 The software Geneious Version 6.1.7r was used for cloning strategy design, sequencing data
900 analysis and sequence alignments. The kinase-specific prediction of phosphorylation sites in
901 zebrafish ASC was carried out using the online software GPS 2.1.1 (*22*), using previously
902 described parameters (*23*). The software Prism Version 6.03 (GraphPad) was used for all
903 statistical analyses and graphs. Raw images were processed using ImageJ/Fiji (NIH) and Imaris
904 x64 7.6.4 (Bitplane, AG).

905 **Supplemental References**

906 1. M. Westerfield, *The Zebrafish Book* (2007).

907 2. F. Ellett, L. Pase, J. W. Hayman, A. Andrianopoulos, G. J. Lieschke, mpeg1 promoter
908 transgenes direct macrophage-lineage expression in zebrafish. *Blood*. **117**, e49–56 (2011).

909 3. D. Sieger, C. Moritz, T. Ziegenhals, S. Prykhozhij, F. Peri, Long-range Ca2+ waves
910 transmit brain-damage signals to microglia. *Dev Cell*. **22**, 1138–1148 (2012).

911 4. C. Hall, M. V. Flores, T. Storm, K. Crosier, P. Crosier, The zebrafish lysozyme C promoter
912 drives myeloid-specific expression in transgenic fish. *BMC Dev Biol*. **7**, 42 (2007).

913 5. B. Fischer *et al.*, p53 and TAp63 promote keratinocyte proliferation and differentiation in
914 breeding tubercles of the zebrafish. *PLoS Genet*. **10**, e1004048 (2014).

915 6. F. Peri, C. Nüsslein-Volhard, Live imaging of neuronal degradation by microglia reveals a
916 role for v0-ATPase a1 in phagosomal fusion in vivo. *Cell*. **133**, 916–927 (2008).

917 7. B. Bajoghli, N. Aghaallaei, T. Heimbucher, T. Czerny, An artificial promoter construct for
918 heat-inducible misexpression during fish embryogenesis. *Dev Biol*. **271**, 416–430 (2004).

919 8. K. M. Kwan *et al.*, The Tol2kit: a multisite gateway-based construction kit for Tol2
920 transposon transgenesis constructs. *Dev. Dyn.* **236**, 3088–3099 (2007).

921 9. A. Emelyanov, S. Parinov, Mifepristone-inducible LexPR system to drive and control gene
922 expression in transgenic zebrafish. *Dev Biol*. **320**, 113–121 (2008).

923 10. A. N. Shah, C. F. Davey, A. C. Whitebirch, A. C. Miller, C. B. Moens, Rapid reverse
924 genetic screening using CRISPR in zebrafish. *Nat Meth* (2015), doi:10.1038/nmeth.3360.

925 11. M. Stemmer, T. Thumberger, M. Del Sol Keyer, J. Wittbrodt, J. L. Mateo, CCTop: An
926 Intuitive, Flexible and Reliable CRISPR/Cas9 Target Prediction Tool. *PLoS ONE*. **10**,
927 e0124633 (2015).

928 12. C. Thisse, B. Thisse, High-resolution in situ hybridization to whole-mount zebrafish
929 embryos. *Nat Protoc*. **3**, 59–69 (2008).

930 13. M. Varela *et al.*, Cellular visualization of macrophage pyroptosis and interleukin-1β
931 release in a viral hemorrhagic infection in zebrafish larvae. *J Virol*. **88**, 12026–12040
932 (2014).

933 14. P. D. Hsu *et al.*, DNA targeting specificity of RNA-guided Cas9 nucleases. *Nat Biotechnol*.
934 **31**, 827–832 (2013).

935 15. M. Eltsov *et al.*, Quantitative analysis of cytoskeletal reorganization during epithelial tissue
936 sealing by large-volume electron tomography. *Nat Cell Biol*. **17**, 605–614 (2015).

937 16. O. Avinoam, M. Schorb, C. J. Beese, J. A. G. Briggs, M. Kaksonen, ENDOCYTOSIS.
938 Endocytic sites mature by continuous bending and remodeling of the clathrin coat. *Science*.
939 **348**, 1369–1372 (2015).

940 17. W. Kukulski *et al.*, Correlated fluorescence and 3D electron microscopy with high
941 sensitivity and spatial precision. *The Journal of Cell Biology*. **192**, 111–119 (2011).

942 18. D. N. Mastronarde, Automated electron microscope tomography using robust prediction of
943 specimen movements. *J. Struct. Biol.* **152**, 36–51 (2005).

944 19. J. R. Kremer, D. N. Mastronarde, J. R. McIntosh, Computer visualization of three-
945 dimensional image data using IMOD. *J. Struct. Biol.* **116**, 71–76 (1996).

946 20. F. de Chaumont *et al.*, Icy: an open bioimage informatics platform for extended
947 reproducible research. *Nat Meth*. **9**, 690–696 (2012).

948 21. I. Belevich, M. Joensuu, D. Kumar, H. Vihinen, E. Jokitalo, Microscopy Image Browser: A
949 Platform for Segmentation and Analysis of Multidimensional Datasets. *Plos Biol*. **14**,

950 e1002340 (2016).

951 22. Y. Xue *et al.*, GPS 2.1: enhanced prediction of kinase-specific phosphorylation sites with
952 an algorithm of motif length selection. *Protein Eng. Des. Sel.* **24**, 255–260 (2011).

953 23. H. Hara *et al.*, Phosphorylation of the adaptor ASC acts as a molecular switch that controls
954 the formation of speck-like aggregates and inflammasome activity. *Nat Immunol*. **14**,
955 1247–1255 (2013).

956

957 **Supplemental tables and figures**

958 **Table S1.** Results of JNK and Syk kinase-specific phosphorylation site prediction in zebrafish
959 ASC by the online software GPS 2.1.1 (*22*).

Position	Code	Kinase	Peptide	Score
38	T	CMGC/MAPK/JNK/MAPK9	RRQEPRVTKSAIEKL	2.211
40	S	CMGC/MAPK/JNK	QEPRVTKSAIEKLKD	1.354
40	S	CMGC/MAPK/JNK/MAPK9	QEPRVTKSAIEKLKD	3
40	S	CMGC/MAPK/JNK/MAPK10	QEPRVTKSAIEKLKD	4
93	S	CMGC/MAPK/JNK	RNTGQSESKGAPSDE	1.333
93	S	CMGC/MAPK/JNK/MAPK10	RNTGQSESKGAPSDE	3.857
152	Y	TK/Syk	KVITNEDYCTIRNKE	1.892
152	Y	TK/Syk/Syk	KVITNEDYCTIRNKE	2.627
152	Y	TK/Syk/ZAP70	KVITNEDYCTIRNKE	2.95
160	T	CMGC/MAPK/JNK	CTIRNKETPQKKMRE	5.104
160	T	CMGC/MAPK/JNK/MAPK8	CTIRNKETPQKKMRE	14.861
160	T	CMGC/MAPK/JNK/MAPK9	CTIRNKETPQKKMRE	3.053
160	T	CMGC/MAPK/JNK/MAPK10	CTIRNKETPQKKMRE	6.429
170	T	CMGC/MAPK/JNK	KKMRELLTGPITCAG	1.521
185	Y	TK/Syk/ZAP70	NKGKEVLYDALRESN	2

960

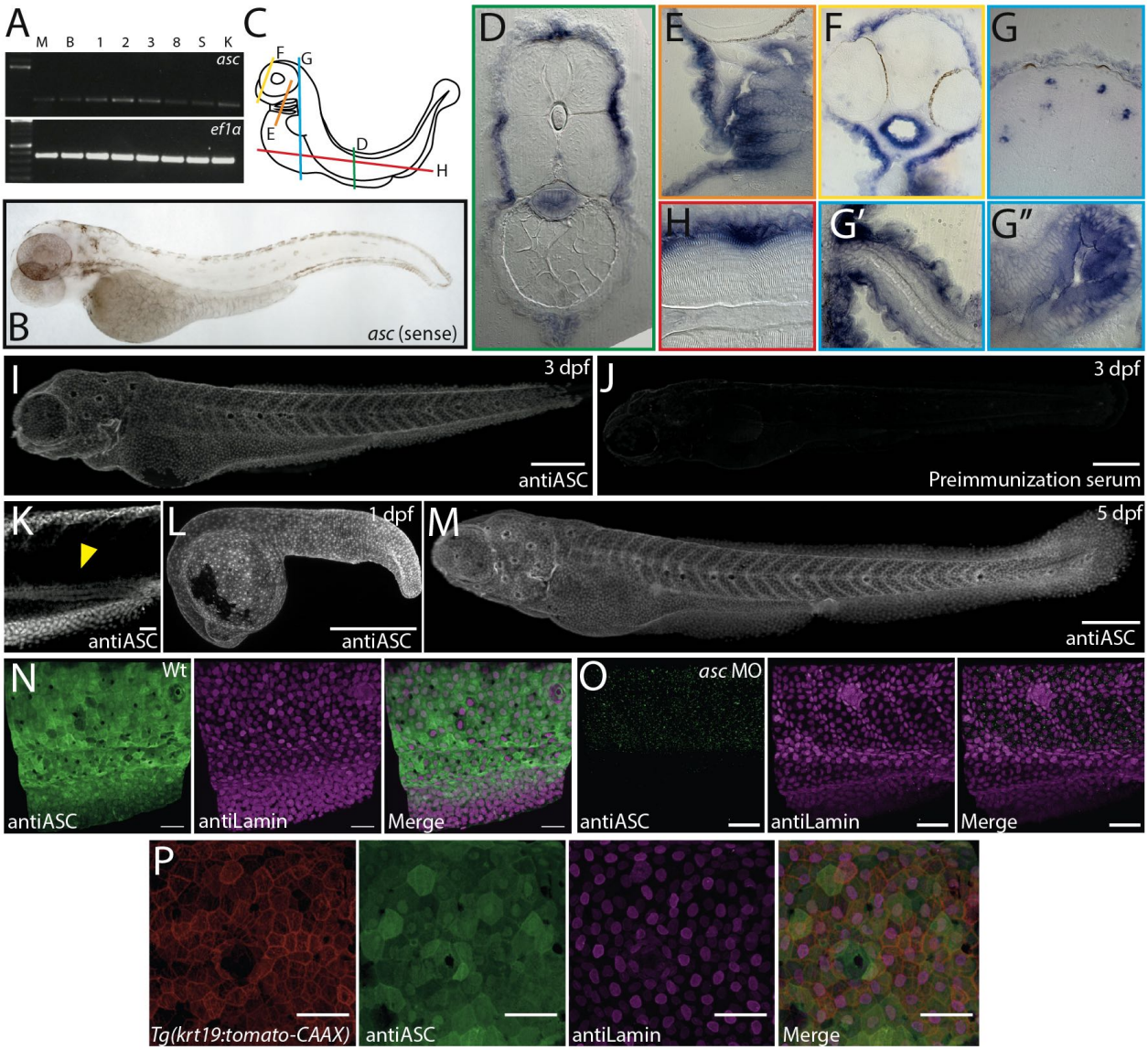

Fig. S1. *asc* is expressed during zebrafish early development. RT-PCR of *asc* during early development in Morula (M), Blastula (B), 1, 2, 3 and 8 dpf, adult spleen (S) and adult head kidney (K). *ef1a* is used as housekeeping gene control [A]. Sense probe control for *asc wish* [B]. Diagram depicting plastic-embedded *asc* (antisense probe) *wish* sample sectioning [C] including trunk cross section [D], enlarged view of gills [E], anterior [F] and posterior [G] head region, lateral fin [G'], intestine [G"] cross sections; and of longitudinal trunk section [H]. Immunostaining in 3 dpf larvae using antiASC [I] or preimmunization serum [J]. Single plane of ASC immunostaining showing expression in intestine [yellow arrowhead, K]. Immunostainings of ASC in 1 dpf embryo [L] and 5 dpf larvae [M]. Immunostainings of ASC in 3 dpf wild type [N] and *asc* ATG-morpholino injected larvae [O]. antiLamin staining is used as positive control. Immunostaining of *Tg(krt19:tomato-CAAX)* transgenic 3 dpf larva shows ASC expression in basal and EVL keratinocytes [P]. Scale bars, 300 µm for full larvae, otherwise 50 µm.

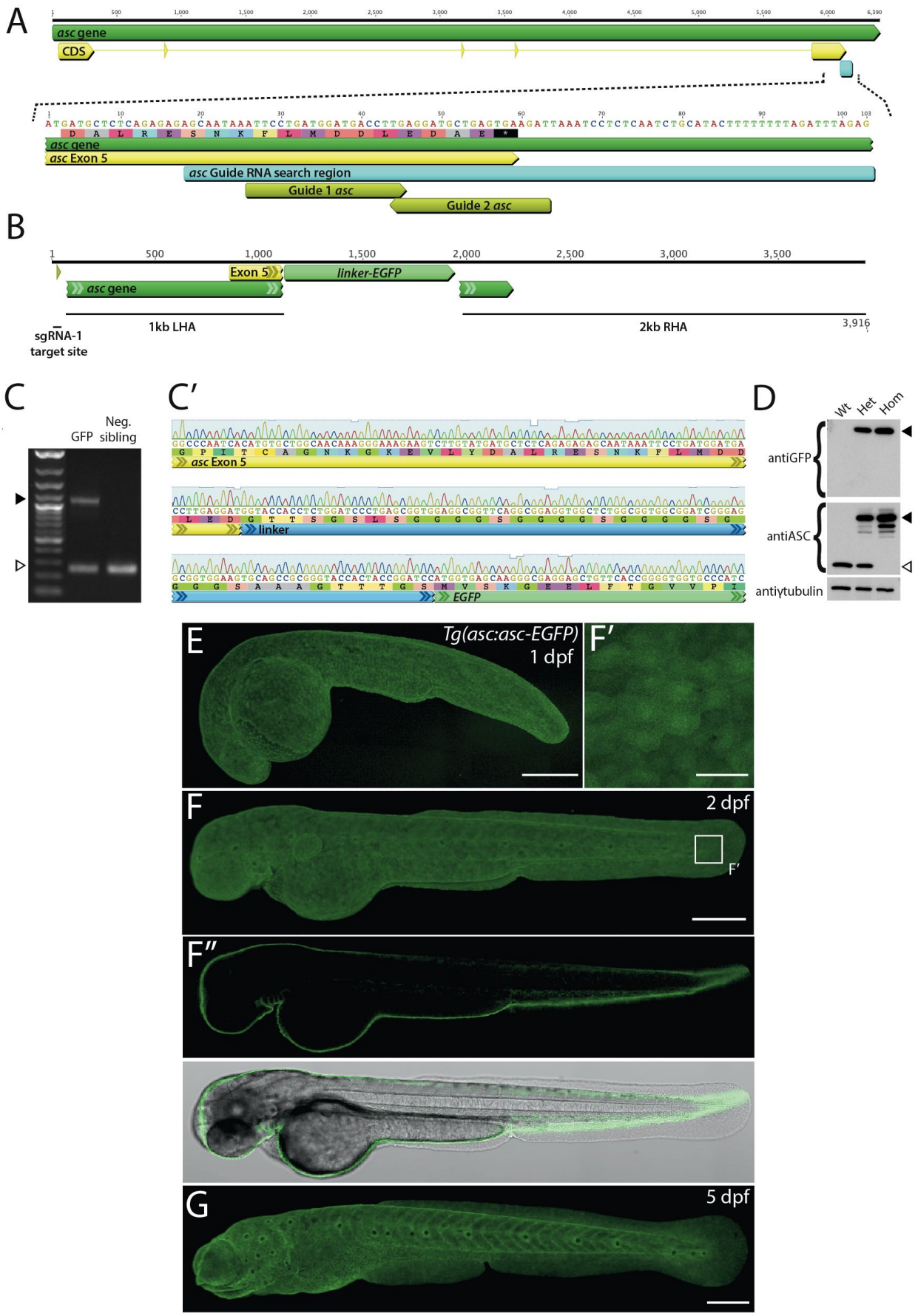

973 **Fig. S2. Generation, genotyping and imaging of *Tg(asc:asc-EGFP)*.** Diagram of *asc* gene

974 (green) with exons (yellow) showing sgRNA search region in final exon (teal) and Guide 1 and

975 Guide 2 *asc* sgRNAs (lime green) [A]. Donor vector design included 1 and 2 kb left and right
976 homology arms (LHA and RHA, respectively) flanking a linker-*EGFP* CDS [B]. Single F1
977 progeny larvae, screened based on GFP expression, were genotyped via PCR using primers
978 flanking the Guide 2 *asc* sgRNA target site. Amplification of the wild type allele yields a 260 bp
979 product (white arrowhead), of *asc-EGFP* allele a 1.1 kb product (black arrowhead) containing the
980 850 bp linker-*GFP* sequence [C]. Sequencing of the 1.1 kb *asc-EGFP* allele PCR product [C'].
981 Western blotting of full protein extracts of wild type, and heterozygous and homozygous
982 *Tg(asc:asc-EGFP)* larvae. GFP is present only in transgenic larvae (black arrowhead). Untagged
983 protein is absent in homozygous *Tg(asc:asc-EGFP)* larvae (white arrowhead) [D]. Live imaging
984 of *Tg(asc:asc-gfp)* at 1 dpf [E], 2 dpf [F] and 5 dpf [G]. Magnification of epidermal cells shows
985 ASC-GFP localization in the nucleus of epidermal cells [F']. Optical sagittal section of 2 dpf
986 larva with and without brightfield merge [F'']. Scale bars, 300 µm for full larvae, otherwise 40
987 µm.

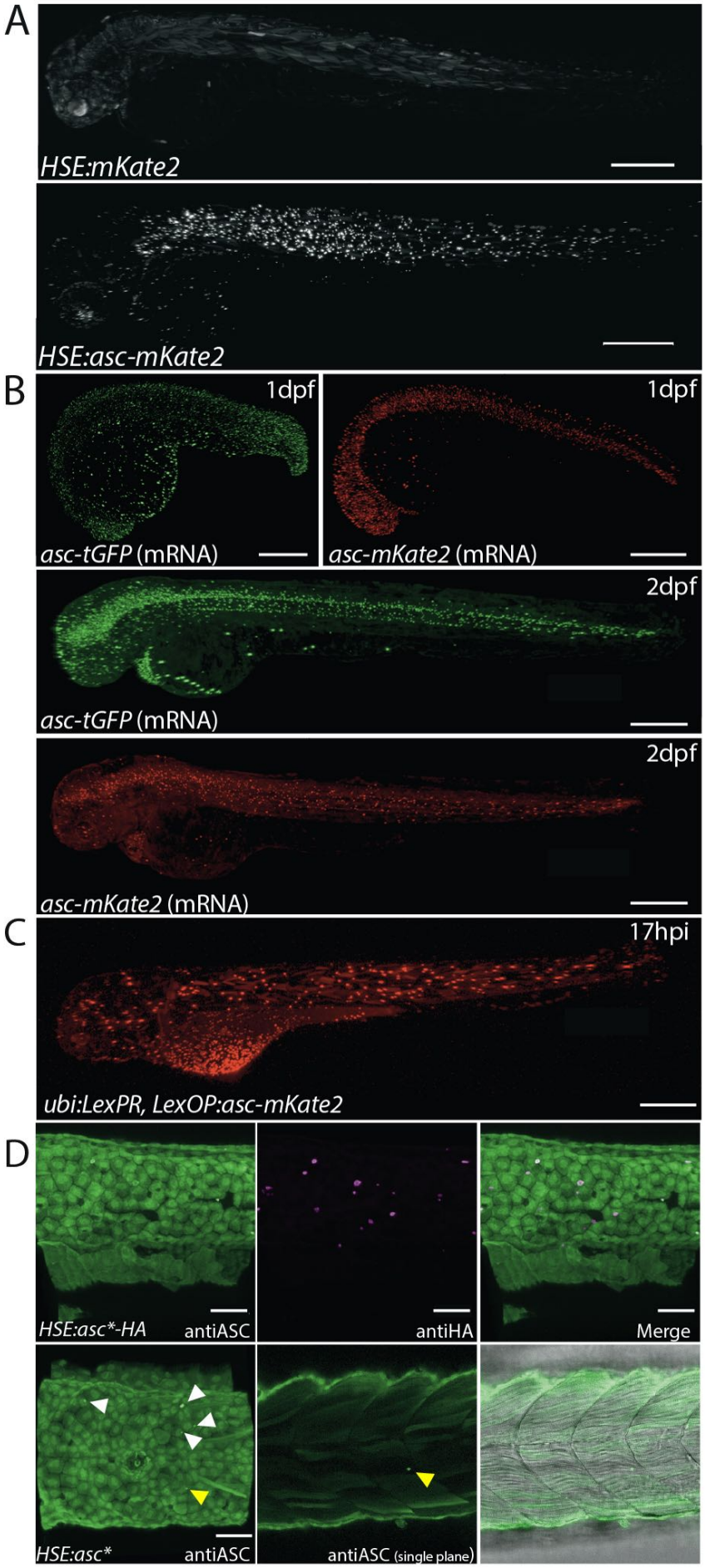
A
HSE:mKate2
HSE:asc-mKate2
B
1dpf
asc-tGFP (mRNA)
1dpf
asc-mKate2 (mRNA)
2dpf
asc-tGFP (mRNA)
2dpf
asc-mKate2 (mRNA)
C
17hpi
ubi:LexPR, LexOP:asc-mKate2
D
HSE:asc*-HA
antiASC
antiHA
Merge
HSE:asc*
antiASC
antiASC (single plane)

988 **Fig. S3. ASC misexpression *in vivo* results in speck formation.** Live imaging of 3 dpf larvae
989 transiently expressing *HSE:mKate2* or *HSE:asc-mKate2* 17 hphs [A]. Specks are only observed
990 after heat shock in larvae expressing ASC-mKate2. Wild type *asc-mKate2* or *asc-tGFP* mRNA
991 injected embryos at 1 and 2 dpf [B]. Live imaging of 3 dpf larvae transiently expressing *asc-*
992 *mKate2* from a LexPR/OP construct driven by the *ubi* promoter. Specks are observed 17h after
993 addition of Mifepristone to the media, which enables LexPR binding to the LexOP operator [C].
994 AntiASC immunostaining of 3 dpf larvae after transiently expressing *HSE:asc-HA* or *HSE:asc*
995 [D]. Specks of ASC-HA are colabeled by antiHA (upper row). ASC specks (untagged) are
996 highlighted by arrowheads (lower row). Scale bars, 300 μm for full larvae, otherwise 50 μm.

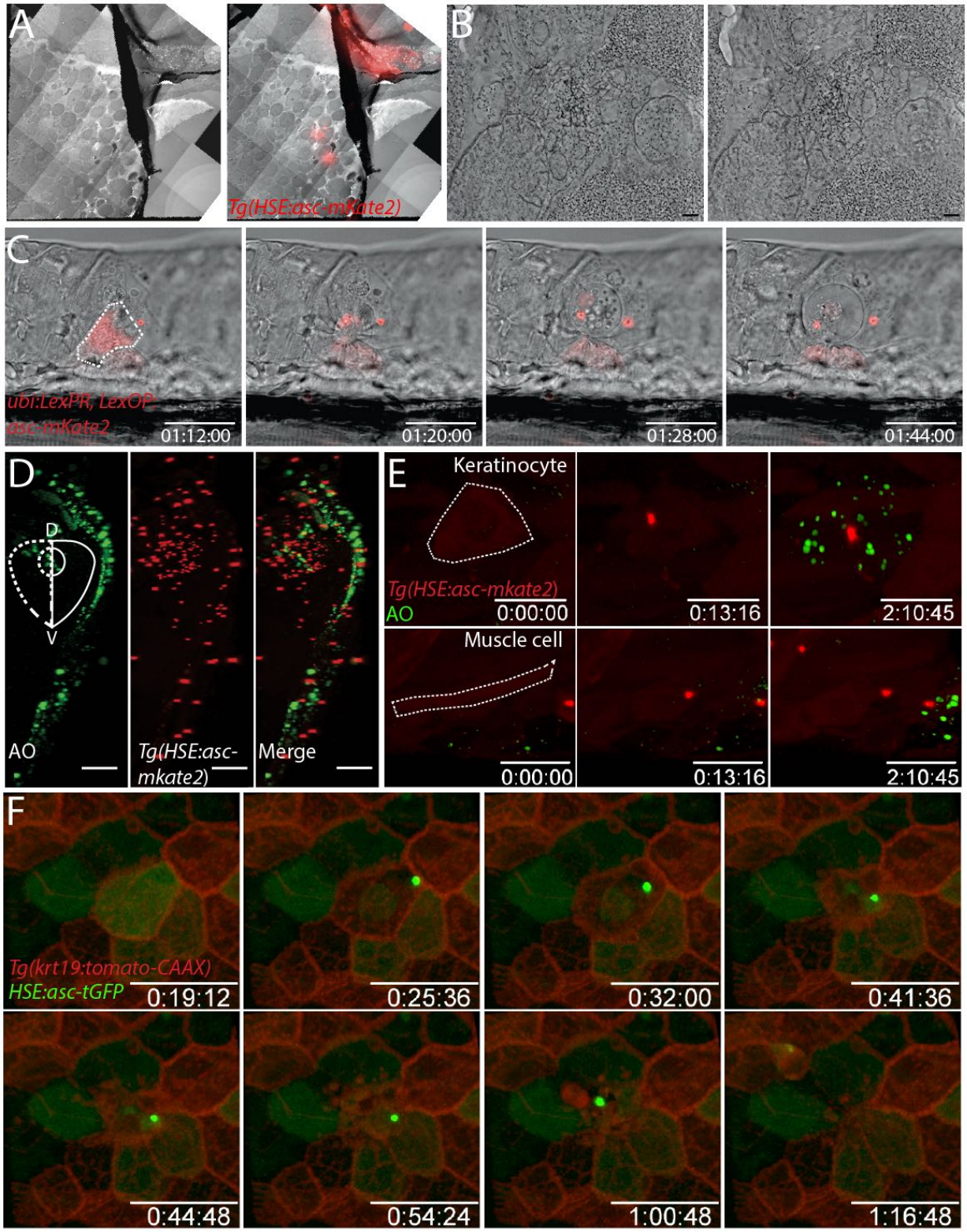

Fig. S4. ASC speck formation leads to keratinocyte cell death. Low magnification of tissue section showing separate electron micrograph and overlay with red channel [A]. TEM tomography slices of second speck, shown in black arrowhead on fig. 4A at two different depths [B]. Scale bars, 200 nm. Live imaging of single keratinocyte transiently expressing Mifepristone-inducted ASC-mKate2 and undergoing cell death after speck formation [C]. Right side of trunk

1002 cross section of 3 dpf *Tg(HSE:asc-mKate2)* larva stained with acridine orange at 15 hphs (D,
1003 dorsal; V, ventral) [D]. Cell death mainly localizes to the epidermal layer. Time lapse imaging of
1004 single keratinocyte and muscle cell in a 3 dpf *Tg(HSE:asc-mKate2)* larva stained with acridine
1005 orange at 3 hphs [E]. Acridine orange-labeled debris accumulates only after speck formation in
1006 the keratinocyte. Time lapse imaging of 3 dpf *Tg(krt19:tomato-CAAX)* larva transiently
1007 expressing *HSE:asc-tGFP*, showing plasma membrane collapse and cell extrusion after speck
1008 formation in keratinocytes [D]. Scale bars, 30 μm.

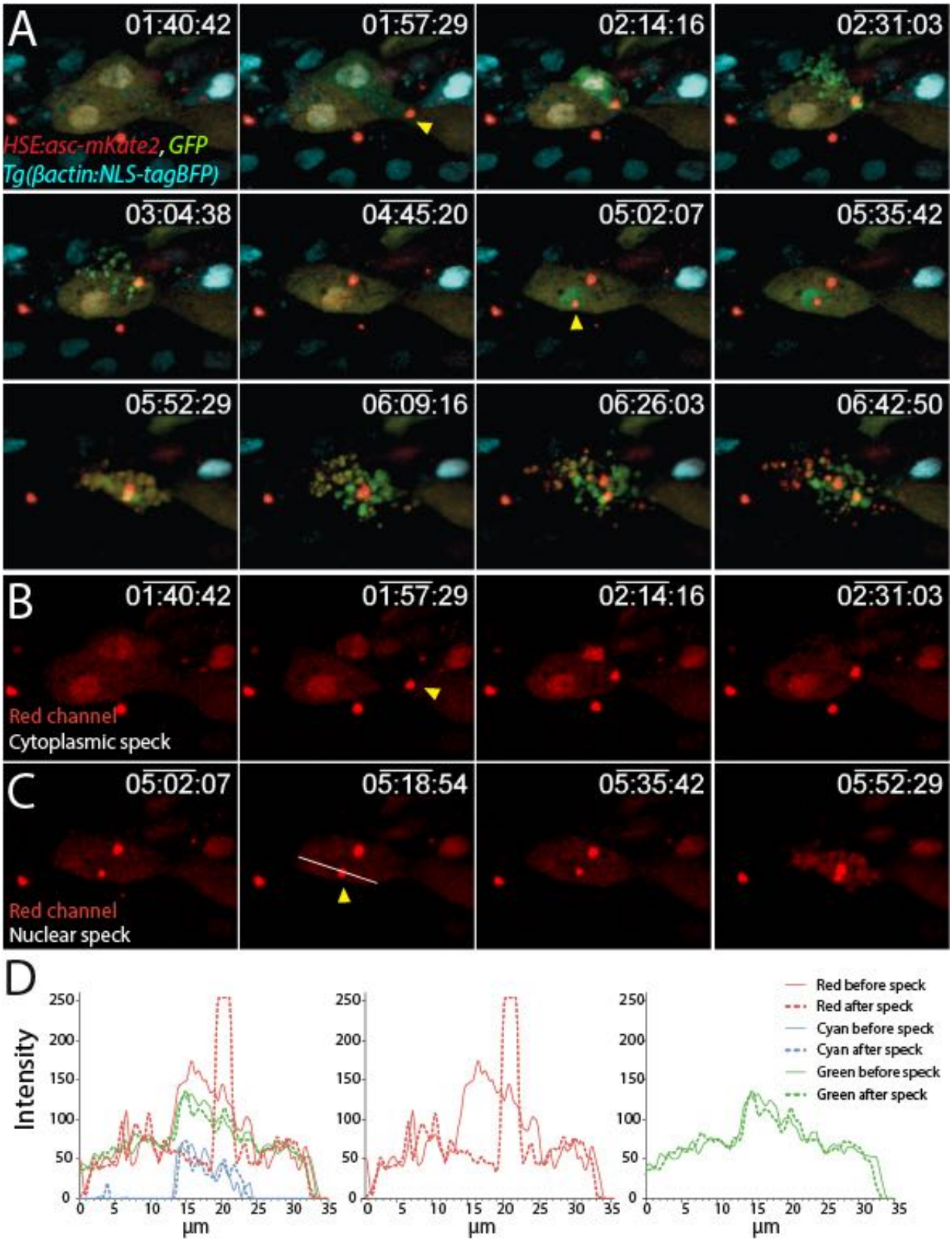

1009 **Fig. S5. Cell death follows speck formation in the nucleus or cytoplasm of keratinocytes.**
1010 Time lapse imaging of transient ASC-mKate2 and GFP expression in *Tg(βactin:NLS-tagBFP)*
1011 larvae 6 hphs [A]. Yellow arrowheads signal speck formation events in two cells; first, within the
1012 cytoplasm and second, within the nucleus. Red channel showing ASC-mKate2 depletion from

1013 cytoplasmic [B] and nuclear compartments [C] during speck formation. Intensity plot profile
1014 (white line) before and after nuclear speck formation for all channels [D]. Middle and right panels
1015 show green and red channels separately, highlighting ASC-mKate2 depletion only from nuclear
1016 pool. Scale bars, 20 µm.

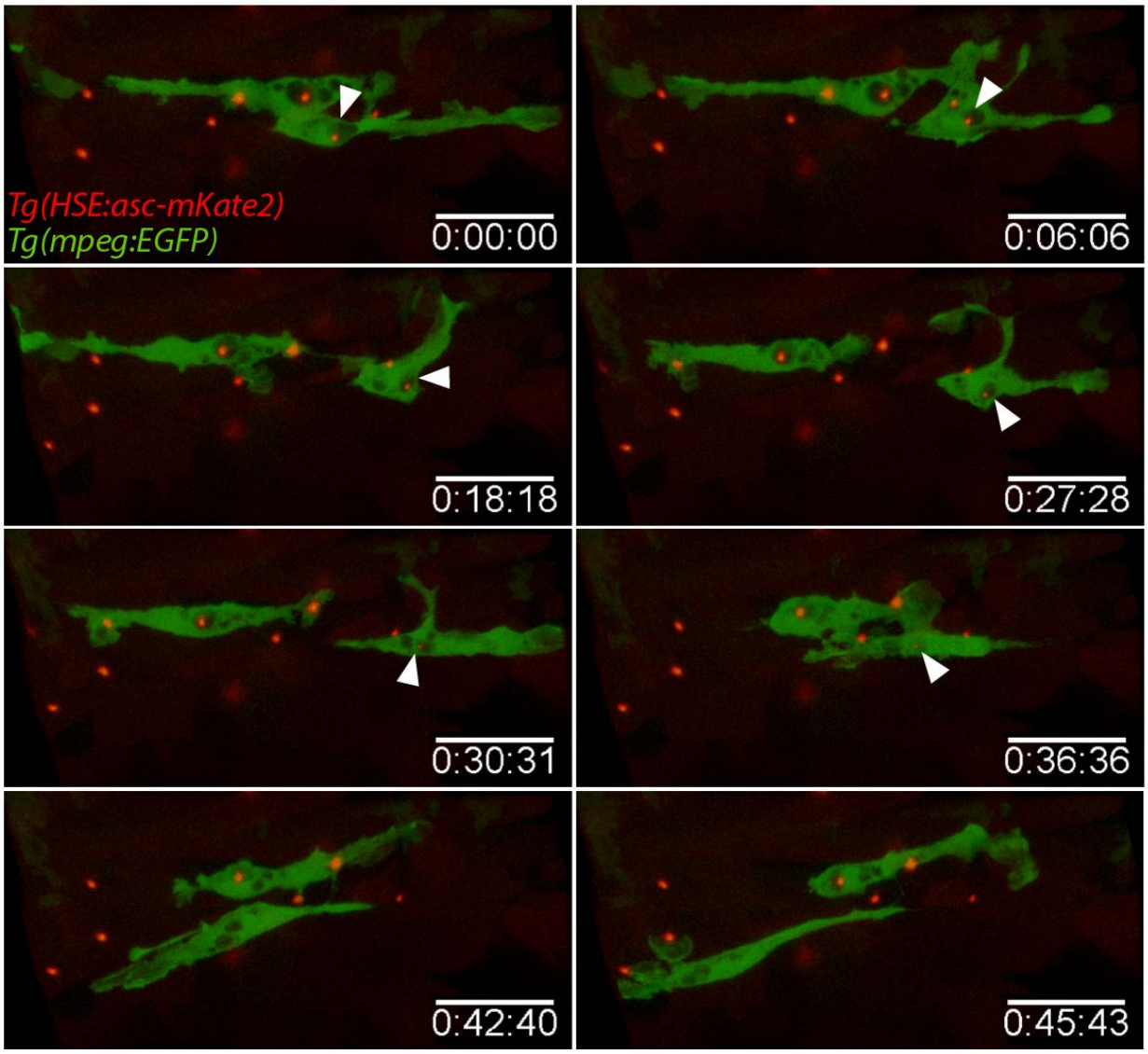

1017 **Fig. S6. ASC specks are degraded within phagosomes.** Time lapse imaging of *Tg(HSE:asc-*
1018 *mKate2, mpeg:EGFP)* larvae 17 hphs, showing degradation of speck within phagosome [white
1019 arrowhead]. Scale bars, 30 µm.

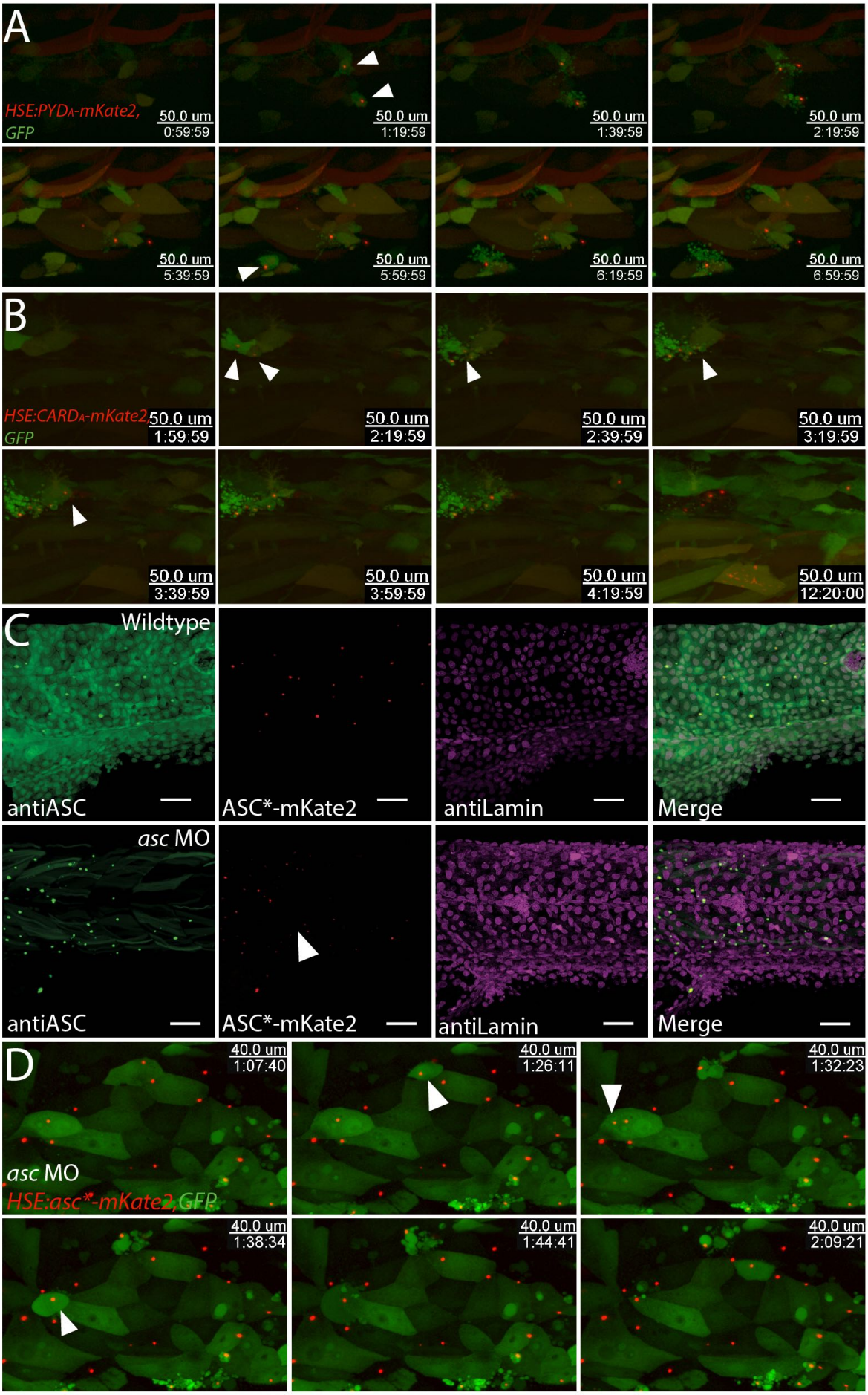
A
HSE:PYDA-mKate2,
GFP
50.0 um
0:59:59
50.0 um
1:19:59
50.0 um
1:39:59
50.0 um
2:19:59
50.0 um
5:39:59
50.0 um
5:59:59
50.0 um
6:19:59
50.0 um
6:59:59
B
HSE:CARDA-mKate2,
GFP
50.0 um
1:59:59
50.0 um
2:19:59
50.0 um
2:39:59
50.0 um
3:19:59
50.0 um
3:39:59
50.0 um
3:59:59
50.0 um
4:19:59
50.0 um
12:20:00
C
Wildtype
antiASC
ASC*-mKate2
antiLamin
Merge
asc MO
antiASC
ASC*-mKate2
antiLamin
Merge
D
40.0 um
1:07:40
40.0 um
1:26:11
40.0 um
1:32:23
asc MO
HSE:asc*-mKate2, GFP
40.0 um
1:38:34
40.0 um
1:44:41
40.0 um
2:09:21

1020 **Fig. S7. In presence of endogenous ASC, PYD_A or $CARD_A$ overexpression leads to speck**
1021 **formation.** Time lapse imaging of keratinocytes transiently expressing *HSE:PYD_A*-mKate2 [A] or
1022 *HSE:$CARD_A$*-mKate2 [B] and GFP in wild type larvae 3 hphs. Specks in keratinocytes are
1023 undistinguishable from those formed by ASC-mKate2 overexpression, and also lead to cell death
1024 (white arrowheads). Immunostaining of 3 dpf larvae expressing morpholino resistant version of
1025 *asc-mKate2* containing 6 silent mutations (*asc*-mKate2*) in wild type [C, upper row] or *asc*
1026 morpholino-injected larva [C, lower row]. Lamin is used as a positive control for the staining.
1027 Time lapse imaging of *asc* morpholino-injected *Tg(asc:asc-EGFP)* larvae transiently expressing
1028 *HSE:asc*-mKate2* with GFP [D]. Speck formation and cell death is unaffected by lack of
1029 endogenous protein. Scale bars, 20 μm.

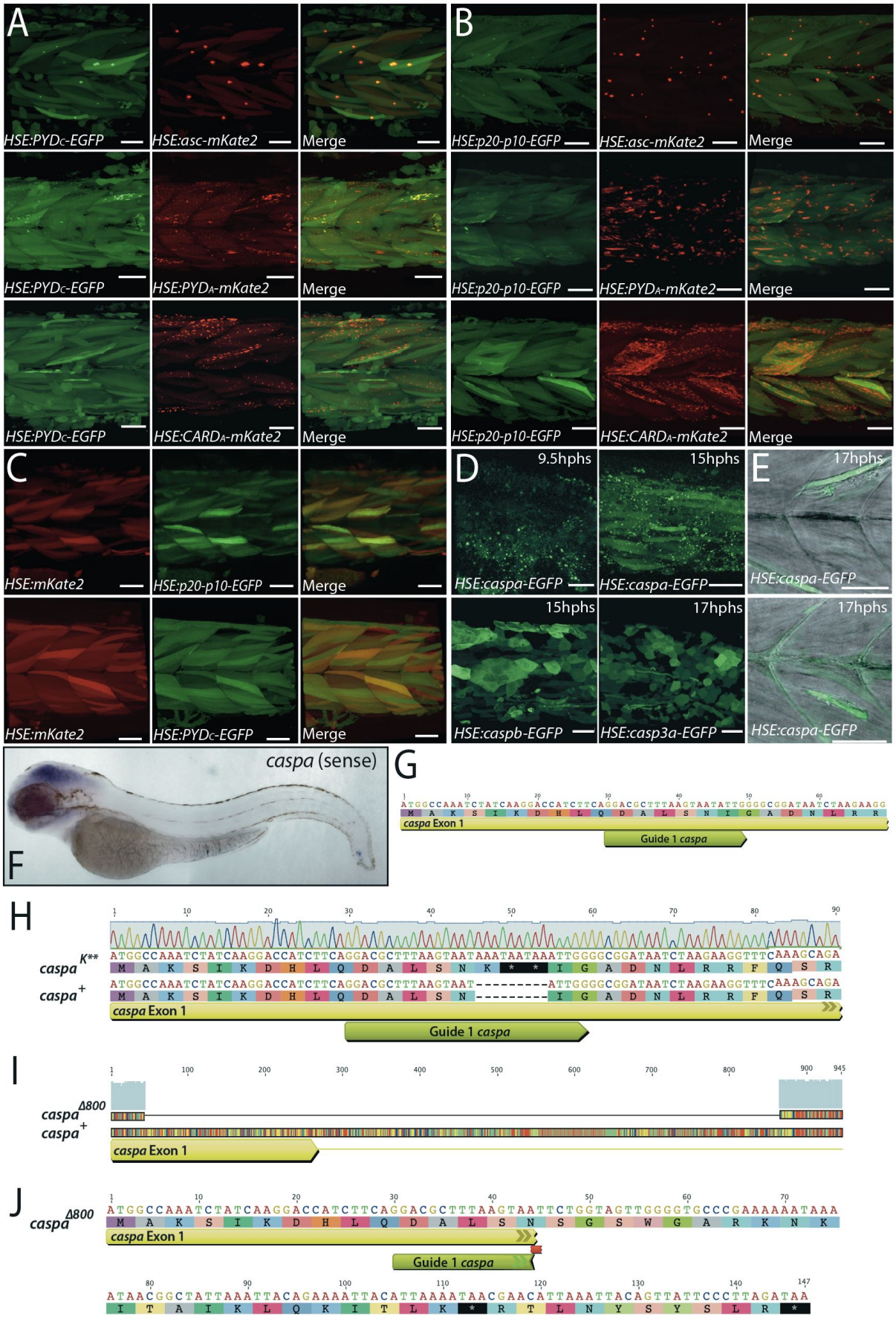

1030 **Fig. S8. Consequences of Caspa overexpression land generation of a *caspa* mutant.** Live

1031 imaging of heat-shock induced transient expression of single Caspa domains: *HSE:PYD$_C$-mKate2*

1032 [A] or *HSE:p20-p10$_C$-mKate2* [B] with full length ASC, its individual domains or mKate2 [C]
1033 around 17 hphs. Interaction only occurs when both proteins contain their respective PYD
1034 domains. Live imaging of transient expression of *HSE:caspa-EGFP*, *HSE:caspb-EGFP* or
1035 *HSE:casp3a-EGFP* between 9 and 17 hphs [D]. Vast amounts of epidermal cellular debris are
1036 seen only when Caspa-GFP is overexpressed. Single plane of *HSE:caspa-EGFP* transient
1037 expression 17 hphs in muscle cells showing morphological changes upon Caspa-GFP
1038 overexpression [E]. Scale bars, 50 µm. Sense probe control for *caspa wish* [F]. Generation of two
1039 *caspa* mutant alleles using CRISPR/Cas9 [G-J]. First exon of *caspa* gene (yellow) with target
1040 sites of Guide 1 *caspa* sgRNA (lime green) [G]. Sequence of *caspa*^{K**} allele: an insertion of 9 bp
1041 adds one lysine (K) and two STOP codons in the *caspa* reading frame [H]. Sequence of caspa$^{\Delta 800}$
1042 allele: deletion of 800 bp fragment containing 224 bp of Exon 1 and 596 bp from Intron 1 [I],
1043 causes frame shift and insertion of a STOP codon after 37 aa [J].

1044 **Supplemental Movies**

1045 **Movie S1.** Time lapse imaging of endogenous speck formation examples in 3 dpf *Tg(asc:asc-*
1046 *EGFP)* larvae.
1047 **Movie S2.** Time lapse imaging of speck formation in 3 dpf *Tg(asc:asc-EGFP)* larva induced by
1048 *HSE:NLR-mKate2* or *HSE:asc-mKate2* transient overexpression.
1049 **Movie S3.** Time lapse imaging of speck formation in 3 dpf *Tg(HSE:asc-mKate2)* full larva in
1050 single cells.
1051 **Movie S4.** TEM tomography stack of specks in 3 dpf *Tg(HSE:asc-mKate2)* larva 18 hphs.
1052 **Movie S5.** Time lapse imaging of speck formation in single muscle cells of 3 dpf *Tg(HSE:asc-*
1053 *mKate2)* larva with brightfield, in EVL keratinocytes of 3 dpf *Tg(HSE:asc-mKate2, krt4:GFP)*
1054 larva without and with brightfield, in keratinocytes 3 dpf *Tg(HSE:asc-mKate2)* with lynGFP-
1055 labeled plasma membrane and in keratinocytes of 3 dpf *Tg(krt19:Tomato-CAAX)* transiently
1056 expressing *HSE:asc-tGFP*.
1057 **Movie S6.** Time lapse imaging of nuclear speck formation in 3 dpf *Tg(asc:asc-EGFP)* larva
1058 expressing *HSE:NLS-asc-mKate2* and 3 dpf *Tg(βactin:NLS-tagBFP)* larvae transiently
1059 expressing *HSE:asc-mKate2* and GFP.
1060 **Movie S7.** Time lapse imaging of *Tg(HSE:asc-mKate2, mpeg:EGFP)* larvae.
1061 **Movie S8.** Time lapse imaging of *HSE:PYD$_A$-mKate2* or *HSE:CARD$_A$-mKate2* and GFP
1062 transiently expressed in 3 dpf wildtype larvae and *HSE:asc-mKate2*, *HSE:PYD$_A$-mKate2* or
1063 *HSE:CARD$_A$-mKate2* and GFP transiently expressed in 3 dpf *asc* morpholino-injected
1064 *Tg(asc:asc-EGFP)* larvae.

1065 **Movie S9.** Time lapse imaging of *HSE:asc-mKate2* and GFP transiently expressed in 3 dpf
1066 wildtype or *caspa* knockout larvae.
1067